THE DE HAAS-VAN ALPHEN

EFFECT AND THE FERMI SURFACE OF THORIUM

by

David Joseph Boyle

A Dissertation Submitted to the

Graduate Faculty in Partial Fulfillment of

The Requirements for the Degree of

DOCTOR OF PHILOSOPHY

Major Subject: Physics

Approved:

In Charge of Major Work

Head/of/Major Department

Dean of Graduate College

Iowa State University
Of Science and Technology
Ames, Iowa

1968

TABLE OF CONTENTS

iii

ABSTRACT

The de Haas-van Alphen effect has been extensively studied in single crystals of thorium, using the field-modulation technique for magnetic fields of 62 kG and temperature of $1.1^{\circ}K$. The quasi-static fields were precisely determined by means of nuclear magnetic resonance, and the dHvA data were recorded digitally for frequency analysis by the periodogram method. The observed frequencies ranged from 2.0 to 25 MG, with the dominant terms in the 9.5-14 MG band. These results were then compared to the frequency variations arising from the Fermi surface proposed by Gupta and Loucks. The experimental observations for the dominant band were in good qualitative agreement with the electron-surface model of twelve butterfly-shaped pieces along the <110> directions. The hole surface suggested by the data consists of a quasi-spherical segment centered at the point Γ of the Brillouin zone, and of dumbbell-shaped pieces with axes along the <111> directions and centered at the symmetry points L.

I. INTRODUCTION

Most of the electrical and magnetic properties of metals can be described in terms of the behavior of the conduction electrons, which obey Fermi-Dirac statistics. These statistics imply that only those electrons with energies near the Fermi energy can take part in ordinary physical processes which involve low transfer of energy. The collection of momentum states corresponding to this Fermi energy is known as the Fermi surface which, at absolute zero, forms a sharp boundary between occupied and unoccupied states in momentum space. Knowledge of the shape of this surface and of its differential properties is a prerequisite for the calculation of most of the physical properties of a metal.

One of the tools which can be used to probe the Fermi surface is the de Haas-van Alphen (dHvA) effect, which consists of oscillations in the magnetization of a single crystal of the metal as the applied magnetic field H is varied. The physical origin of these oscillations will be discussed later, but the important feature is that the frequency F of these oscillations (which are periodic in reciprocal field) is related to the extremal cross sectional area $\mathcal{A}_f$ of the Fermi surface normal to the field direction by the Onsager relation (1952)

$$F(\underline{H}) = \frac{\hbar}{2\pi e} \mathcal{A}_f(\underline{H}) \quad . \tag{1.}$$

Knowledge of the dHvA frequencies for all field directions thus leads directly to a knowledge of Fermi-surface cross-sections for all directions, and to an understanding of the size and shape of the entire Fermi surface. However, the dHvA effect can be observed only when the electrons can travel unscattered through the crystal lattice for one or more of their

cyclotron orbits, imposing the experimental conditions of low temperatures ($\sim 1^\circ K$), high magnetic fields ($H \sim 50$ kG), and single crystal samples of high physical and chemical perfection.

This thesis is concerned with a study of the dHvA effect in thorium, and with the interpretation of the experimental data in terms of a model Fermi surface. Thorium, with an atomic number of 90, is the first element in the actinide series of the periodic table, the outer electrons of which are in the 5f, 6d, and 7s shells. The crystal structure at room temperature is the face-centered-cubic α-phase, with a lattice constant of 5.084 Å, and at $1360^\circ C$ there is a transition to the body-centered-cubic β-phase before reaching the melting point. The melting temperature depends markedly on impurity content, and has been recently determined to be $1750^\circ C$, by extrapolating melting-point measurements on a series of alloys with carbon to zero carbon content (Dooley, 1966).

The outer electron configuration in the free thorium atom is $6d^2 7s^2$; all the heavier elements in the actinide series retain the $7s^2$ shell, with varying degrees of occupancy of both the 5f and 6d shells, resulting in partially filled energy bands for the metal.

Because of the difficulty of obtaining thorium in sufficient purity, previous experimental data on its electronic properties have been rather inconclusive. Even the room-temperature electrical resistivities reported by various investigators have ranged from 13 to 25 μohm-cm; the room-temperature value extrapolated to zero carbon content by Dooley (1966) is 15.0 ± 0.2 μohm-cm. Due to its even valence and cubic symmetry, thorium must be regarded as a "compensated" metal, having the same number of

conduction electrons and holes, i.e., the volume of the hole Fermi surface ↙

should equal that of the electron surface. No experimental data on the

magnetoresistance and the Hall effect are available to support this view,

although Berlincourt's (1959) measurements at low fields on rather impure

polycrystalline samples do not contradict it. Berlincourt found a

constant Hall coefficient and a magnetoresistance proportional to H^2,

situations which would be expected to occur in a compensated metal.

Lehman (1959) calculated the electronic band structure of the acti-

nides by means of a Kohn variational principle applied to a linear combi-

nation of atomic orbitals, and he discovered that the location of the

5f bands was particularly sensitive to the type of interatomic potential

used. Prophetically he asserted that the accuracy of the energy eigen-

values for the actinide metals could not be guaranteed unless the calcula-

tions were carried out self-consistently. Lehman's band-structure calcu-

lations incorporated relativistic effects by inclusion of the spin-orbit

coupling term, but were for the 6d bands only, since he considered the

5f and 7s bands to be of less importance. He also calculated the bands

without spin-orbit coupling, and found these non-relativistic bands to

resemble those of paramagnetic nickel, as determined some years earlier

by Fletcher and Wohlfarth (1951). The main features of the Fermi surface

proposed by Lehman are summarized in Table 1.

More recently, Keeton and Loucks (1966) have calculated energy bands

for thorium using the relativistic augmented-plane-wave (RAPW) method

and taking into account the 6d and 7s bands, although still neglecting

bands derived from the 5f states. The Fermi energy was calculated to be

0.481 Ry, and the resulting density of states $N(\epsilon_F)$ at the Fermi level was compared with available electronic specific heat data (see Table 1). Keeton and Loucks cautioned that the experimentally derived value of $N(\epsilon_F)$ might be too large, due to the electron-phonon enhancement effect. The Fermi surface proposed by Keeton and Loucks was quite different from that found by Lehman, principally because of a hole surface made up of multiply connected rings. However, these calculations were recently found to be unreliable since Loucks (1967)[1] discovered that the Keeton-Loucks "6d" bands had been inadvertently derived from 5f levels, the positions of which were quite sensitive to potential.

More recently, Gupta and Loucks (1968) have proposed a revised band structure for thorium, in which more careful consideration was given to the 5f bands. In these calculations, the 5f bands were found to lie above the d bands, which reduced their effect on the Fermi surface and suggested that the behavior of the conduction electrons in thorium would be less actinide-like and more similar to transition metals such as paramagnetic nickel. The value $N(\epsilon_F)$ determined by Gupta and Loucks (see Table 1) is in reasonably good agreement with that calculated from the specific heat coefficient γ found from two studies of superconductivity in thorium, one by Gordon, Montgomery, Noer, Pickett, and Tobón (1966), and the other by Decker, Peterson, and Finnemore (1967). The latter group measured critical field curves for thorium samples of

---

[1]Loucks, T. L., Physics Department, Iowa State University of Science and Technology, Ames, Iowa. Importance of 5f levels in thorium band structure calculations. Private communication. 1967.

Table 1. Comparison between theory and experiment of density of states $N(\epsilon_F)$ at the Fermi surface

THEORY Source	Lehman (1959)	Keeton & Loucks (1966)	Gupta & Loucks (1968)
Fermi surface	Hole ellipsoids along Γ X, Γ K Electron ellipsoids along Γ L Electron pocket at Γ	Electron surface at Γ Hole surface of multiply connected rings	Hole surface centered at Γ, multiply connected along Γ L Electron surfaces on Γ K
$N(\epsilon_F)$ states/spin/Ry·atom		21 ± 4	13.5 ± 3.5
EXPERIMENT Source		Clusius & Franzosini (1956)	Gordon et al. (1966) Decker et al. (1967)
γ cal/mole·deg^2		16.4×10^{-4}	10.3×10^{-4}
$N(\epsilon_F)$ states/spin/Ry·atom		19.8	12.4

relatively high purity, and found them to be in excellent agreement with the BCS theory.

The Fermi surface inferred from the Gupta-Loucks bands consists of a hole surface centered at the point Γ in the Brillouin zone and shaped like a rounded cube with multiply-connected arms along the $\langle 111 \rangle$ Γ L directions, and a symmetry-related set of electron surfaces located roughly halfway along ΓK, with the longest dimension perpendicular to ΓK and in the (100) plane. This model will be examined in greater detail when discussing the results gained from the present dHvA experiments.

The dHvA effect in thorium was first observed by Thorsen, Joseph, and Valby (1967), using the impulsive-field method with a maximum usable field of 180 kG. Because their thorium crystals were relatively impure, with resistivity ratios $\rho_{300°K}/ \rho_{4°K}$ <100, the effect was difficult to detect. Their measurements of the dHvA period P = 1/F for the field directions lying in the (110) and (100) planes are presented in Figure 1., which shows the dHvA frequencies confined to two bands, one extending from 9.7 MG to 12.8 MG, and the other from 19.2 MG to 25 MG^2.

Thorsen et al. found the lower-frequency oscillations to be dominant especially near [110], but because of the difficulties introduced by the presence of complicated beat patterns, these authors quoted an uncertainty of roughly 5% for much of their data. This set of low-frequency oscillations was attributed to extremal cross-sectional areas of "bumpy ellipsoids"

---

[2]We shall express dHvA frequencies in MG=10^6 G=10^6cycles/(gauss)$^{-1}$, since the oscillations are periodic in reciprocal field.

FIGURE 1: Previous determinations of the dHvA periods in thorium (after Thorsen, Joseph, and Valby, 1967), with the corresponding dHvA frequencies in MG noted on the right-hand side of each plot. The error bars signify scatter among data taken on various samples.
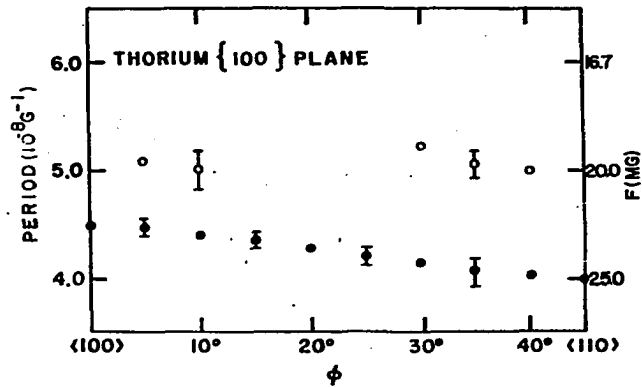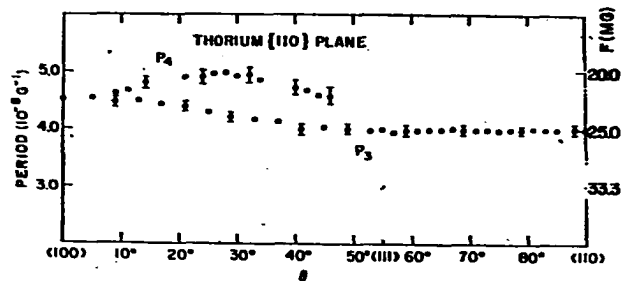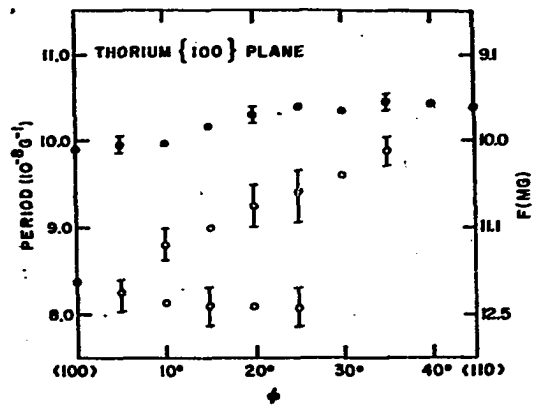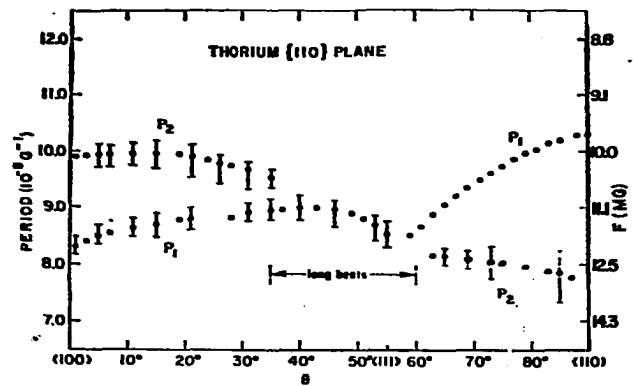
centered on the points X of the Brillouin zone. However, as Thorsen et al. noted, the period of the dominant branch labelled P_1 in Figure 1 varied approximately as the cosine of the angle from [110], suggestive that the relevant portion of the Fermi surface should in fact be more like a cylinder than the bumpy ellipsoid. Anomalous disappearances of the data, such as for the branch P_2 near [110], were attributed to spin-splitting effects.

Turning now to the higher frequencies, Thorsen et al. found them to be nearly isotropic with angle, and ascribed them to a quasi-spherical Fermi surface centered at Γ, with appropriate bumps and indentations to give rise to two or more extremal areas for a given field direction, as seemed to be required by the beat patterns which were observed. The volumes of the two sheets of Fermi surface were estimated to be approximately equal, but Thorsen, Joseph, and Valby pointed out that other undetected pieces of Fermi surface might conceivably exist.

With the development of thorium crystals of high purity at this laboratory (Peterson, Schmidt, and Verhoeven, 1966), and in light of the continuing theoretical calculations mentioned above, a further study of the dHvA effect in thorium was considered to be very desirable. In the following two chapters of this thesis, we shall discuss the modulated-field technique which was used for the detection of the dHvA effect, details of the apparatus used, and the methods of data analysis. In Chapter IV, the dHvA frequency and effective-mass data will be presented, and an interpretation of these data will be discussed with reference to the Gupta-Loucks model in Chapter V.

II. THE DE HAAS-VAN ALPHEN EFFECT AND ITS MEASUREMENT

In the presence of a magnetic field, conduction electrons in metals travel in quasi-helical paths, the axis of the "helix" being parallel to the field. The energy associated with the periodic motion at right angles to the field is analogous to the quantization of the Bohr orbits of the hydrogen atom. As far as momentum is concerned, the effect of a magnetic field $\underline{H}$ is to constrain the allowed states to lie on a set of tubes whose areas $\mathscr{A}_n$ projected on the plane perpendicular to $\underline{H}$ are quantized according to Onsager's (1952) rule

$$\mathscr{A}_n = \frac{2\pi eH}{\hbar} (n + \gamma) \quad , \quad n = 0, 1, 2, \ldots , n', \tag{2.}$$

where γ is close to 1/2 (Chambers, 1966). As H increases, the quantized tubes expand until $\mathscr{A}_{n'}$ is just equal to $\mathscr{A}_F$, an extremal cross-sectional area of the Fermi surface, at which point this outermost tube becomes depopulated, and the electron energy distribution becomes rearranged with the electrons occupying states of lower quantum number. Thus, every time that n' changes by unity, the free energy of the system undergoes a small fluctuation, which is reflected as a fluctuation in the magnetization; the frequency F of these fluctuations in reciprocal field is given in Equation 1.

A detailed expression for the amplitude of the oscillatory part of the free energy associated with a single extremal area was first derived by Lifshitz and Kosevich (1956) (see Gold (1968) for a review of the theory). Their final result for the free energy may be written as

$$\Omega_{osc} = -(\frac{H^2}{2\pi F})D(\underline{H}) \sum_{r=1} \frac{X_r}{\sinh X_r} \frac{K_r}{r^{5/2}} \cos (2\pi r(F/H-\gamma)\mp \frac{\pi}{4}) \qquad (3.)$$

where:

$D(\underline{H})$ is an amplitude factor $\alpha H^{1/2}$,

$$X_r = 2\pi^2 rm^* k_B T/e\hbar H \quad , \qquad\qquad (4.)$$

$$K_r = \exp(-2\pi^2 rm^* k_B T_D/e\hbar H) \quad ,$$

and where T is absolute temperature, T_D is the "Dingle temperature" which heuristically describes the amplitude reduction due to lattice imperfections, m^* is the cyclotron effective electron mass, and k_B is Boltzmann's constant. The oscillatory magnetization is then given by

$$\underline{M}_{osc} = -\nabla_{\underline{H}} \Omega_{osc}$$

$$= D(\underline{H}) [\hat{\underline{H}} - \frac{1}{F}\frac{\partial F}{\partial \theta}\hat{\underline{\theta}} - \frac{1}{F \sin \theta}\frac{\partial F}{\partial \phi}\hat{\underline{\phi}}]$$

$$\qquad\qquad\qquad\qquad\qquad\qquad\qquad\qquad (5.)$$

$$\times \sum_r \frac{X_r}{\sinh X_r} \frac{K_r}{r^{3/2}} \sin (2\pi r(F/H - \gamma)\mp \pi/4) \quad ,$$

which we write for short as

$$\underline{M}_{osc} = \sum_r \underline{M}_{osc}^r = \sum_r \underline{A}_r (\underline{H},F_r) \sin (2\pi F_r/H + \beta_r) \quad , \qquad (6.)$$

where the subscript r has now been taken to include all dHvA frequencies which may be present for a given field direction $\hat{\underline{H}}$, as well as all

harmonics associated with each extremal area (Equation (3.)). It should be noted that the vector $\underline{M}^r_{osc}$ will not be parallel to $\underline{H}$ unless $\underline{H}$ happens to be along a symmetry direction, for which both $\partial F_r/\partial\theta$ and $\partial F_r/\partial\phi$ vanish.

In this work, the magnetic field was provided by a 62-kG superconducting solenoid, together with a small modulating field of amplitude ~100 G, and the effect was detected as an oscillatory e.m.f. induced in a pickup coil surrounding the crystal as the field from the superconducting solenoid was slowly varied. If the main quasi-static field is denoted by $\underline{H}_o$, and the modulation field is written as $\underline{h}\sin\omega t$, the total field applied to the sample is $\underline{H}_t = \underline{H}_o + \underline{h}\sin\omega t$. Because of the intrinsic non-linearity of the function $\underline{M}_{osc}(\underline{H}_t)$, the induced e.m.f. will be rich in harmonics of the modulation frequency ω, i.e., the voltage across the pickup coil will consist of terms whose time-frequencies are ω, 2ω, 3ω, etc.

If $\underline{h}$ is not parallel to $\underline{H}_o$, the modulation will cause small changes not only in the amplitude, but also in the direction, of $\underline{H}_t$, with similar small changes in the direction of $\underline{M}_{osc}$. Since any $\underline{\theta}$-component of $\underline{M}^r_{osc}$ is due to the nonvanishing factor $\partial F_r/\partial\theta$, the detected amplitude for oblique modulation should depend on $\partial F_r/\partial\theta$, as can be seen explicitly by expansion of the numerator and denominator of the sine in Equation (6.). To first order in h/H_o, we have

$$H_t^{-1} = (\underline{H}_t \cdot \underline{H}_t)^{-1/2} \doteq \frac{1}{H_o} (1 - \frac{\underline{H}_o \cdot \underline{h}}{H_o^2} \sin \omega t)$$

$$\hat{\underline{H}}_t = \underline{H}_t (H_t^{-1}) = \hat{\underline{H}}_o + \frac{\sin \omega t}{H_o^3} (\underline{H}_o \times (\underline{h} \times \underline{H}_o)) \tag{7.}$$

$$F_r(\hat{\underline{H}}_t) = F_r(\hat{\underline{H}}_o) + \frac{\sin \omega t}{H_o^3} (\underline{H}_o \times (\underline{h} \times \underline{H}_o)) \cdot \nabla_{\theta, \Phi} F_r(\hat{\underline{H}}_o) \quad,$$

so that

$$\underline{M}_{osc}^r = \underline{A}_r(\underline{H}_t) \sin \left[\frac{2\pi F_r(\underline{H}_t)}{H_t} + \beta_r \right] \tag{8.}$$

becomes

$$\underline{M}_{osc}^r = \underline{A}_r(\underline{H}_o) \sin \left[\frac{2\pi F_r(\hat{\underline{H}}_o)}{H_o} + \beta_r - \frac{2\pi F_r(\hat{\underline{H}}_o)}{H_o^2} h_{eff} \sin \omega t \right] \tag{9.}$$

where

$$h_{eff} = h \left[\hat{\underline{H}}_o \cdot \hat{\underline{h}} - \frac{(\hat{\underline{H}}_o \times (\hat{\underline{h}} \times \hat{\underline{H}}_o))}{F_r(\hat{\underline{H}}_o)} \cdot \nabla_{\theta, \Phi} F_r(\hat{\underline{H}}_o) \right] \tag{10.}$$

is an effective modulation amplitude. The first term in the brackets gives the component of the modulation in a direction parallel to $\underline{H}_o$, whereas the term involving $(\hat{\underline{H}}_o \times (\hat{\underline{h}} \times \hat{\underline{H}}))$ gives the component perpendicular to $\underline{H}_o$, which does indeed involve the factors $\partial F_r / \partial \theta$ and $\partial F_r / \partial \Phi$. A means of frequency elimination then presents itself: the direction of $\underline{h}$ can be chosen to make h_{eff} zero for a selected frequency F_r, regardless of the magnitude of $\underline{h}$.

Equation (9.), which shows the specific dependence of the magnetization on the modulation frequency ω, can be expanded into harmonics of ω because of the nonlinear (i.e., trignometric) dependence on $\sin \omega t$. In the experimental apparatus a multiple n of the modulation frequency ω is used as a reference signal to a lock-in amplifier detecting the e.m.f. produced in the pickup coil. If the term $z_r = 2\pi F_r(\hat{\underline{H}}_o)h_{eff}/H_o^2$ is much less than 2π, the output of the amplifier should be proportional to the nth field derivative of $\underline{M}_{osc}^r$ (i.e., to $\dfrac{\partial^n}{\partial \underline{H}_o^n} A_r(\underline{H}_o)\,\sin\!\left[\dfrac{2\pi F_r(\hat{\underline{H}}_o)}{H_o}+\beta_r\right]$).

However, it is actually advantageous to increase the amplitude of h_{eff} so that $z_r \gtrsim 2\pi$, in order to fully exploit the nonlinear character of the dHvA response to the magnetic field (Stark, 1967; Windmiller and Priestley, 1965; Stone, 1967). Since the oscillations are periodic in reciprocal field, it follows that $H_o^2/F_r(\hat{\underline{H}}_o)$ is equal to ΔH, the field spacing for one dHvA cycle, and setting $z_r \sim 2\pi$ thus amounts to choosing the modulation amplitude h_{eff} to be comparable to ΔH. By choosing a sufficiently low frequency ω of the modulation field, the skin depth (i.e., penetration of field) greatly exceeds sample size, so that the field can be regarded as uniform throughout the crystal; in the present experiments on thorium, the modulation frequency was less than 100 Hz, and from knowledge of the low temperature resistivity, we conclude that the skin depth was greater than 3 cm, which was about ten times the sample size.

Under these conditions, e.m.f. induced in the pickup coil can be written explicitly in terms of ω and its harmonics by expanding the sine in Equation (9.) and then taking the Fourier transform of the

result. The final result is

$$\underline{M}_{osc} = \sum_r \underline{A}_r(\underline{H}_o) \left\{ \sin\left[\frac{2\pi F_r(\hat{\underline{H}}_o)}{H_o} + \beta_r\right] J_0 (z_r) \right.$$

$$\left. + \sum_{n=1}^{\infty} 2 J_n (z_r) \sin\left[\frac{2\pi F_r(\hat{\underline{H}}_o)}{H_o} + \beta_r + \frac{n\pi}{2}\right]\cos n\omega t\right\} , \tag{11.}$$

where J_n is a Bessel function of the first kind of order n, and the argument is $z_r(\underline{H}_o,\underline{h}) = 2\pi F_r(\hat{\underline{H}}_o)h_{eff}/H_o^2$, as before. If $\hat{\underline{\mu}}$ is a unit vector along the axis of the pickup coil, the e.m.f. induced in the coil becomes

$$V = \frac{d}{dt} (\underline{M}_{osc} \cdot \hat{\underline{\mu}}) \tag{12.}$$

$$= - \sum_r \hat{\underline{\mu}} \cdot \underline{A}_r(\hat{\underline{H}}_o) \sum_{n=1}^{\infty} J_n(z_r)\sin\left[\frac{2\pi F_r(\hat{\underline{H}}_o)}{H_o} + \beta_r + \frac{n\pi}{2}\right] 2 n\omega \sin n\omega t ,$$

so that if the reference frequency of the lock-in amplifier is set to the nth harmonic of ω, the output signal is proportional to

$$\sum_r \hat{\underline{\mu}} \cdot \underline{A}_r(\underline{H}_o) 2n\omega J_n(z_r) \sin (2\pi F_r(\hat{\underline{H}}_o)/H_o + \beta_r + \frac{n\pi}{2}) . \tag{13.}$$

This dependence of the amplitude on the Bessel function is another effective means of discrimination among dHvA oscillations of various frequencies F_r. If the electronics of the system can be arranged such that $z_r = 2\pi F_r h_{eff}/H_o^2$ is kept constant as H_o varies slowly with time, the value of z_r and the order of the Bessel function can be chosen to zero the amplitude of a set of dominant oscillations and thus permit the observation of weaker ones. For the conditions of this experiment, the dominant frequency was of the order of 10 MG, and in a typical

applied field of 5×10^4 G, the value of the argument of the Bessel

function turns out to be $2\pi \times 10^7 \, h_{eff}/(5 \times 10^4)^2 \doteq 2.5 \times 10^{-2} \, h_{eff}$.

Thus if h_{eff} were set to 200 G, the value of the argument would be 5,

and since $J_2(5) \doteq 0$, there would be zero response from the 10 MG

oscillations at the second harmonic of the fundamental frequency (n = 2).

On the other hand, if the argument z is chosen to be much less than

that for which $J_n(z)$ reaches its first maximum, we have

$$J_n(z) \propto z^n \quad . \tag{14.}$$

Under these conditions of low-amplitude modulation, the higher

frequency oscillations will have larger amplitude relative to those of

lower frequency, but it is clearly impractical to reduce z indefinitely.

Quite apart from varying the amplitude and direction of the modula-

tion field, the axis of the pickup coil can also be used to discriminate

between dHvA frequencies. It is clear from Equation (12.) that the

optimum pickup occurs when $\underline{\mu}$ is parallel to $\underline{M}_{osc}$ which, as we have already

remarked, is not necessarily along the field direction. Consider fre-

quency branches $F_1(\theta)$ and $F_2(\theta)$, which cross at a particular angle θ_o,

as shown in Figure 2. (a.). The factors $\partial F_1/\partial \theta$ and $\partial F_2/\partial \theta$ are of opposite

sign at this angle, leading to different directions of $\underline{M}^1_{osc}$ and $\underline{M}^2_{osc}$

as indicated in Figure 2. (b.). It is possible to choose $\underline{\mu}$ to be

perpendicular to either $\underline{M}^1_{osc}$ or $\underline{M}^2_{osc}$ and thereby to eliminate one of

these terms, or to be perpendicular to both $\underline{M}^1_{osc}$ and $\underline{M}^2_{osc}$, if other

frequencies with noncoplanar $\underline{M}^r_{osc}$ are to be studied.

FIGURE 2: Illustrating the discrimination of frequency branches by variation of the direction of the pickup coil.

(a.) A schematic representation of two dHvA frequency branches F_1 and F_2, with a crossing point at angle θ_0.

(b.) A sketch of the directions of magnetization arising from these frequency branches. The directions are different because of different θ-components (proportional to $\partial F_r / \partial \theta$) for each vector $\underline{M}^r_{osc}$.

$$\frac{\partial F_1}{\partial \theta} > 0$$

$$\frac{\partial F_2}{\partial \theta} < 0$$

a.

b.
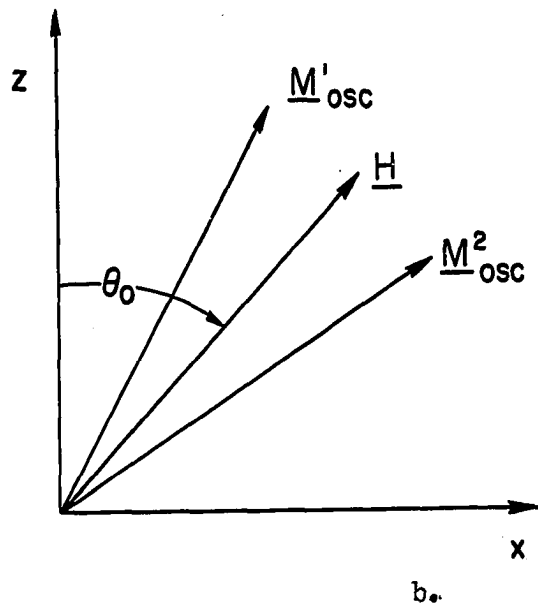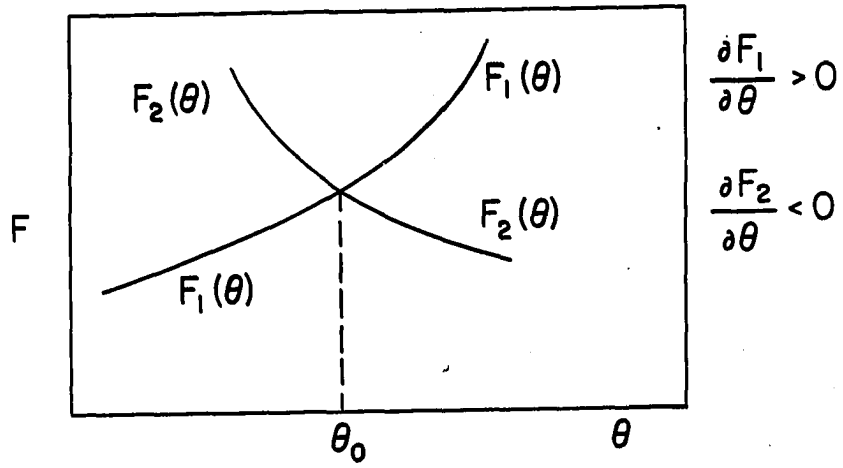
A final technique of frequency discrimination is afforded by conventional filtering techniques applied to the output of the lock-in amplifier. If the rate of change of the main field is $\dot{H}_o$, the time frequency of the dHvA oscillations will be $2\pi F_r \dot{H}_o/H_o^2$. If $\dot{H}_o$ is a constant, the time frequency of the dHvA effect (not to be confused with the time frequency of the modulation field) decreases with increasing H_o. But if the field can be ramped as $H_o = k/t$, then $\dot{H}_o/H_o^2 = 1/k$, and the time frequency of the dHvA oscillations remains constant. Selected dHvA terms can then be amplified or attenuated by conventional ultra-low-frequency filters, since their time-frequencies $2\pi F_r/k$ are all different.

In summary, three independent means of dHvA frequency discrimination are available:

1.) variation of the directions of the modulation field and of the pickup coil, to exploit $\partial F/\partial\theta$ and $\partial F/\partial\phi$ differences for various branches;

2.) variation of the amplitude of the modulation field h_{eff} in proportion to H_o^2, and making use of the Bessel-function response;

3.) changing the field H_o in proportion to the reciprocal of time, in order to use electronic narrow-band filtering.

It is also possible to obtain magnetization oscillations by holding the magnitude of $\underline{H}_o$ constant and varying its direction. If $F_r(\hat{\underline{H}}_o)$ changes with $\hat{\underline{H}}_o$, as it will for any Fermi surface which is not a perfect sphere, the argument of $\sin (2\pi F_r(\hat{\underline{H}}_o)/H_o)$ in Equation (9.) now varies with orientation, and one complete cycle will be recorded every time

that F_r changes by the amount H_o. This behavior permits the tracking of a dHvA frequency through a wide angular range with better relative precision than would be gained from field sweeps at close intervals of angle (Shoenberg and Stiles, 1964). Figure 3 illustrates this effect with reference to an ellipsoidal Fermi surface. As the field is rotated, the extremal cross-sectional area increases, and more quantized tubes can be accomodated with the Fermi surface; a "rotation" oscillation is observed each time a new tube is added (or subtracted).

The static-field rotation method has its limitations, however. Since it cannot detect the <u>direction</u> of change of frequency with angle, field sweeps are needed at angular intervals to determine the <u>sign</u> of $\partial F/\partial\theta$. Furthermore, the rotation method is less useful for weak terms, because it is difficult to zero a dominant term (e.g., by the dependence on the Bessel function) if its dHvA frequency is changing appreciably as the field direction is varied.

FIGURE 3: An illustration of Onsager's (1952) quantized-tube model, as applied
to an ellipsoidal Fermi surface. The effect of a magnetic field $\underline{B}$
on the electron states is to arrange them into tubes in momentum
space; the projected area of the nth tube upon the plane normal to
the field direction is given by $\mathcal{A}_n = \dfrac{2\pi eB}{\hbar}(n + \gamma)$. As the field B

increases, these areas grow, and a fluctuation in the free energy of
the system occurs each time that the cross-sectional dimensions of
a tube exceed those of the Fermi surface. On the other hand, if the
field is held constant in magnitude but is rotated in direction, the
maximum cross-sectional area of the Fermi surface increases, as shown
in succeeding views from left to right. An oscillation is recorded
for every change in this area by $2\pi eB/\hbar$, since another tube is then
permitted within the Fermi surface.
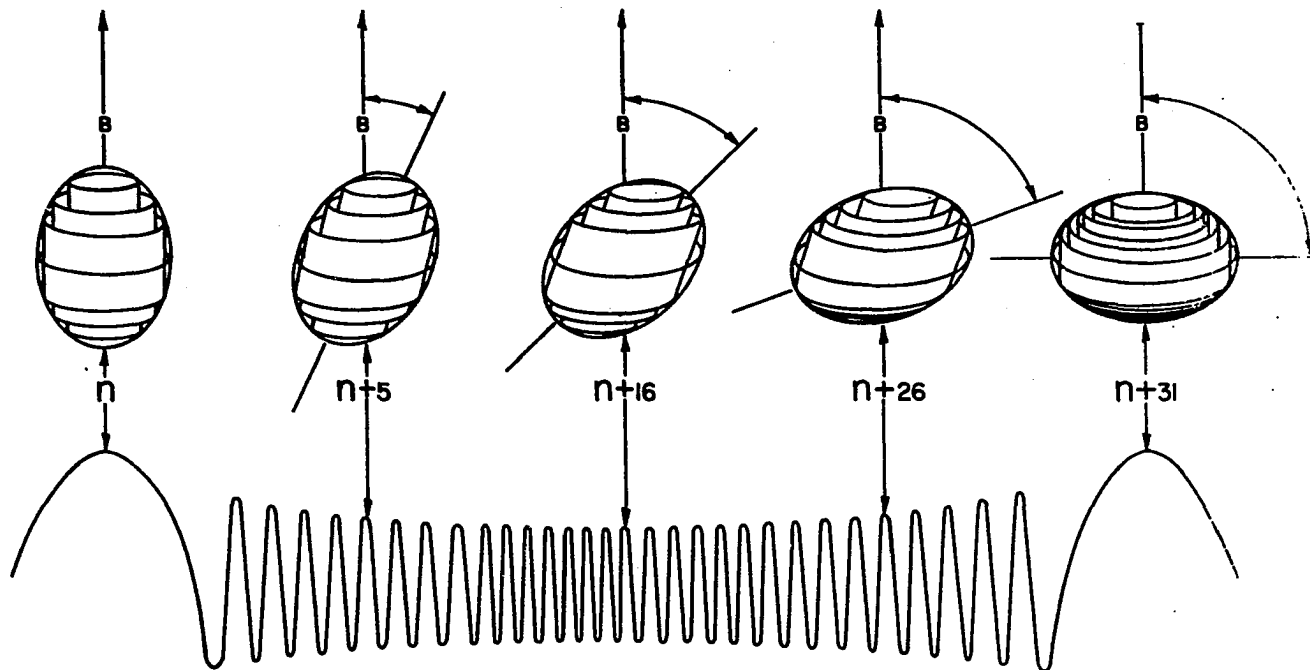
$$\Delta \mathcal{A} = (2\pi e / \hbar c) \, |\underline{B}| = \text{constant}$$

III. EXPERIMENTAL PROCEDURE

3.1 Apparatus

The quasi-static magnetic field for this experiment was provided by a Varian Associates one-inch-bore 62 kilogauss superconducting solenoid driven by a Varian X-4102 20-ampere power supply with a 1/H drive option. The magnet was enclosed in a liquid-nitrogen-jacketed dewar, and was supported by a structure consisting in part of a fiberglas insulator. The current leads to the solenoid were in the form of copper ribbons along the insulator, which allowed them to be cooled by the boiloff gas from the helium bath. With the support structure in place, the liquid helium loss rate was determined to be 300 cc/hr at zero field.

To improve field uniformity, the main solenoid was compensated by additional superconducting coils carrying currents of 1 ampere or less. A "curvature" control on the power supply enabled the amount of current passing through both shimming coils to be varied, and a "z-gradient" control permitted variation of the current through one coil relative to the other. At a specified field (such as 50 kG), the homogeneity could be adjusted to be as little as 3 parts in 10^5 over a 1-cm sphere; but, for the same settings of the shimming controls, the homogeneity deteriorated for other field values in the 35 kG-60 kG range. The field profile for various values of the main field and settings of the compensating current was mapped by use of a fluxball probe and integrator loaned by Varian Associates. These calibrations revealed an additional field component due to "trapped flux", leading to a dished profile for ramping up in field and a domed profile for ramping down, for identical values

of the compensating current (see Figure 4). In practice, a value was chosen which resulted in roughly the same homogeneity for either direction of field ramp, the homogeneity remaining within 1 part in 10^4 over a 1-cm sphere for the duration of data accumulation.

A bar of thorium had been refined by Dr. D. T. Peterson of the Metallurgy Department, using an electrotransport process in which impurities (such as hydrogen, carbon, and oxygen) were moved to one end of the bar by means of a direct current of ~2000 amperes. The starting material of electron-beam-zone-refined thorium was strained by swaging it into a rod about 15 cm in length and 0.25 cm in diameter. For a 96-hour period, the rod was heated by the current to near its melting temperature in a vacuum of 2×10^{-7} Torr, and the relief of the strains aided in the formation of crystals. The current was then reduced to 1700 amperes, and the bar was allowed to anneal at a temperature just below the b.c.c.-f.c.c. transition point, resulting in material with a final measured resistivity ratio $\rho_{300^\circ K}/\rho_{4.2^\circ K}$ of 160. (Thorium of a higher resistivity ratio has been reported (Decker, Peterson, and Finnemore, 1967), but it was in the form of a polycrystalline strip which was not usable for dHvA studies.) The bar described above was composed of many crystallites about 1 mm square or smaller, but two crystals were found to extend through its complete diameter. After being spark-cut out and electropolished, the crystals were roughly cylindrical in shape, with a diameter of 2 mm and a length of 2 or 3 mm, with their monocrystalline character being verified by x-ray diffraction.

The longer crystal was mounted in sample holder SP-1, and the

FIGURE 4: Typical homogeneity data for the field of the super-
conducting solenoid, as taken with the Varian flux-
ball and integrator. The field profile tends to
"dish" for ramping up, and to "dome" for ramping
down. In an effort to counteract this hysteresis-
like effect, the upper right profile was taken at
a different setting of the compensating current.

FIELD RAMPING UP   FIELD RAMPING DOWN

43.5 kG

43.4 kG

49.6 kG

49.7 kG

55.5 kG

56.6 kG

3 cm

10 G

3 cm
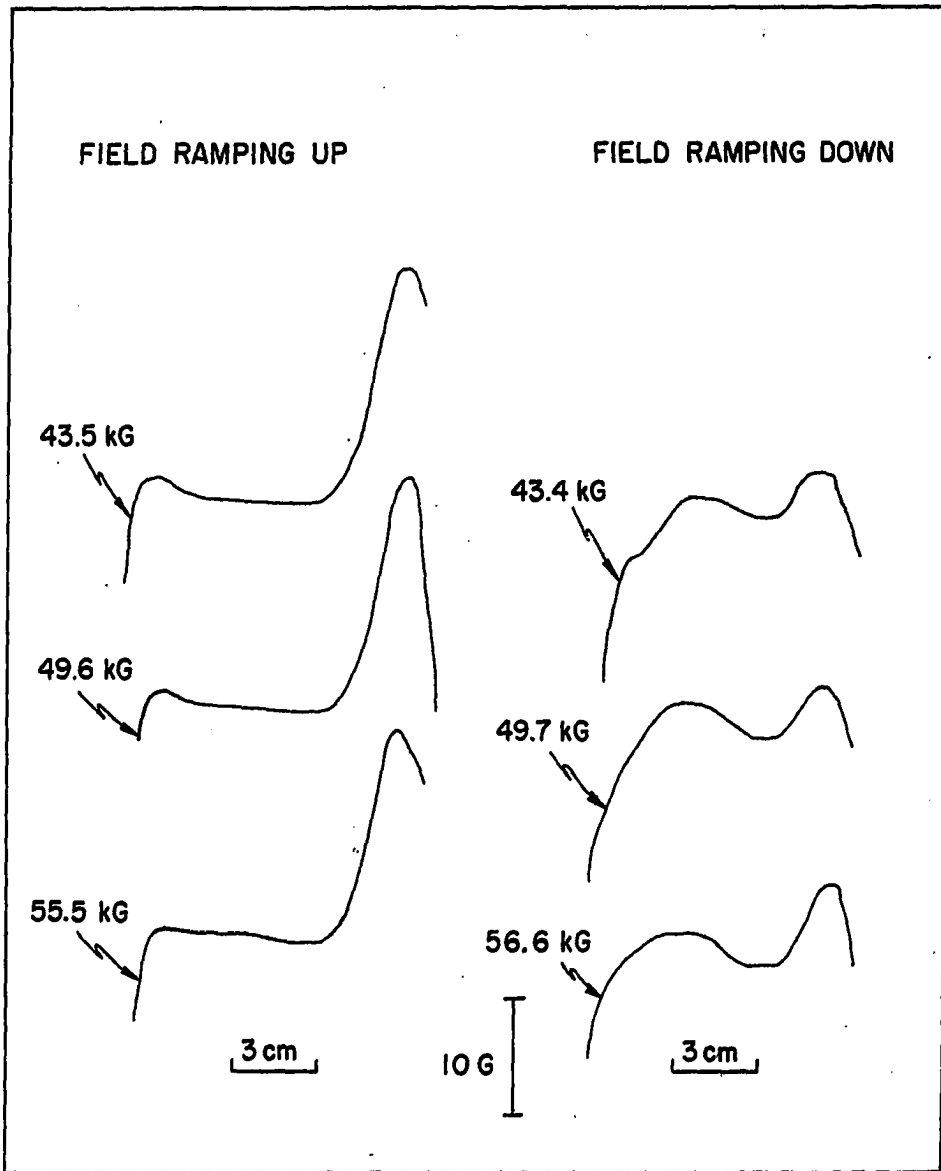
shorter in sample holder SP-2, both of which have been described by Stone (1967). Sample holder SP-2 (shown in Figure 5) carried a nuclear magnetic resonance (n.m.r.) specimen for direct measurement of the applied magnetic field, and was used for the majority of the data taken. Sample holder SP-2 was also preferred because of its reproducibility of angle settings, determined to be within 0.2° after adjustment for back-lash. The wire-driven sample holder SP-1 was prone to stretching and bending of the wire, and absolute angles measured by it were considered to be reliable to $\pm 1^{\circ}$. Flexing of the stainless steel driveshaft in SP-2 was overcome by attaching guides to the main support shaft, and friction was minimized by the use of teflon-tape bushings and teflon-suspension spray on the bearing surfaces. The worm was made of Kel-F to counteract differential contraction, and the bottom of it was anchored with a 2-56 nylon screw, to prevent vertical motion during rotation.

The crystal orientation in SP-2 could be checked by x-ray diffraction as it was mounted in its experimental position. The observed crossing of the intermediate dHvA frequency branches at the [110] and [100] orientations in the (100) plane provided a confirmation of the mounting technique for rotations in the (110) plane. The sample was found to have been mounted within 1° in SP-2, but within 5° in SP-1, as evidenced by a pronounced splitting in the dominant frequencies.

A shortcoming of the worm-gear sample holder was its limited angular range. A prototype was made of a wire-driven sample holder incorporating a rotating pickup coil, which would have an angular range of 360° or more; in addition, its increased wheel diameter should lessen angle

FIGURE 5: An expanded view of the worm-gear sample holder SP-2.

COAXIAL CABLE TO
MARGINAL OSCILLATOR

SAMPLE SUPPORT

THORIUM SAMPLE

n.m.r
COIL

PICKUP COIL
& SPACER

STAINLESS STEEL
TUBING DRIVE

ROTATING
WHEEL

TEFLON
BUSHING

KEL-F WORM

MODULATION
COIL

ANCHORING
SCREW
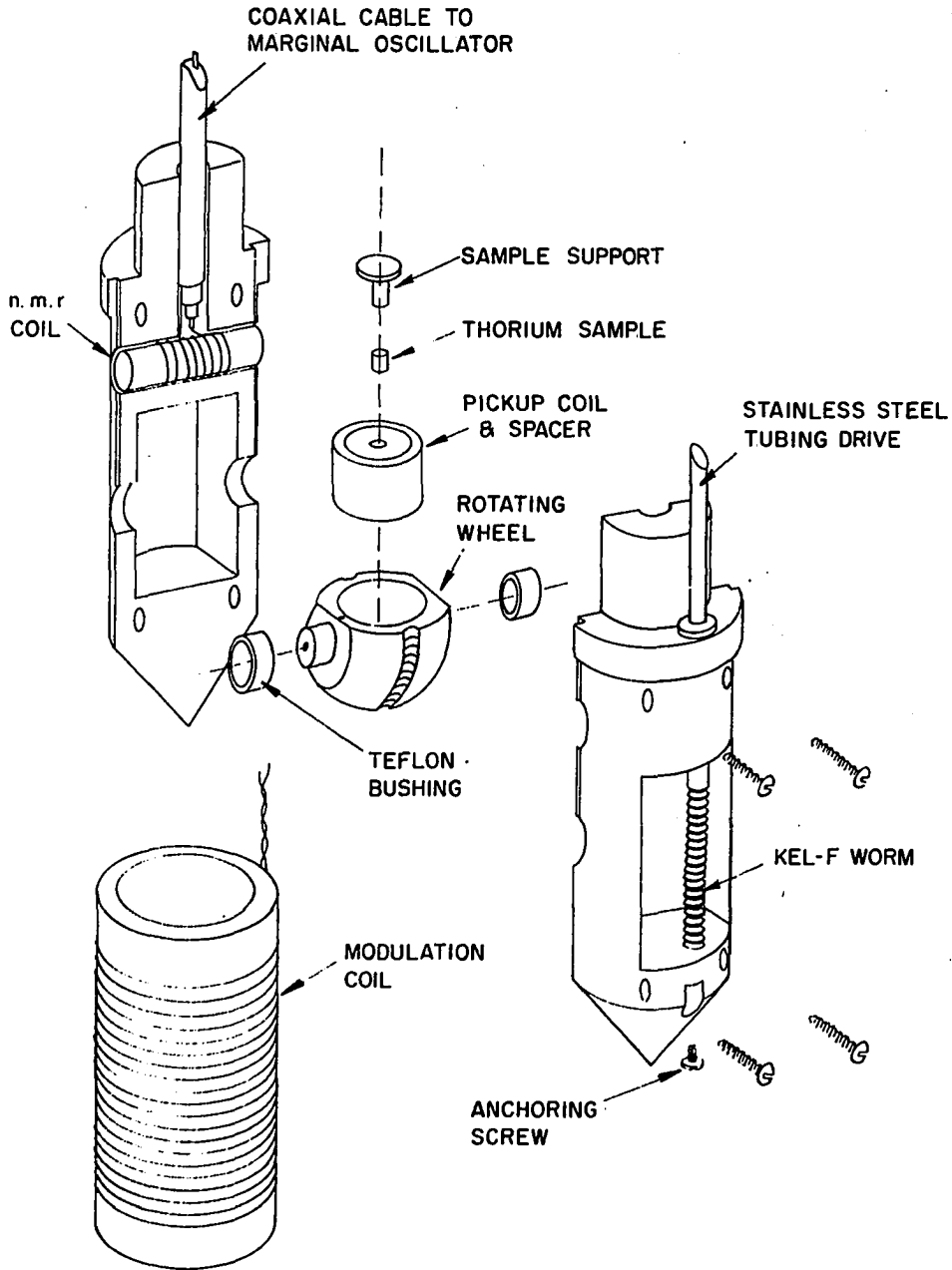
errors caused by irregularities in the driving wire.

The modulation coil of SP-2 was wound with 500 turns of number 38 AWG copper wire, and the pickup coil consisted of 2600 primary and 1700 compensating turns of number 46 AWG wire. The crystal, mounted on a Kel-F support, was placed in the pickup coil and spacer, and this assembly was inserted into the rotating wheel.

The n.m.r. source used was the Al^{27} resonance of 11.1118 MHz/10 kG, using aluminum powder (particles of 15 μ diameter or less) encapsulated in a Teflon tube wound with 9 turns of number 32 AWG copper wire. The marginal oscillator described by Stone (1967) was used, with the addition of a 0.01 μf capacitor across the n.m.r. coil input, which enabled the range of the marginal oscillator to be extended to the 40 - 68 MHz interval with a single connecting cable, thereby eliminating tedious changes of coaxial cable formerly needed to tune the oscillator to the desired frequency (Hill and Hwang, 1966). The n.m.r. coil was connected to the coaxial fitting at the sample holder top by means of "Plaxial" cable (United-Carr Mfg., Newton Highlands, Massachusetts), which used an outer conductor of 0.001" copper plated to the polyethylene dielectric, in order to minimize noise and heat loss while retaining the flexibility of a coaxial cable.

The current to the solenoid passed through a 0.01-ohm, 100-amp Leeds and Northrup standard resistor, and the voltage across it was measured by a Leeds and Northrup 8687 potentiometer, with a specified error of 0.05%. Comparisons of n.m.r. frequency and solenoid current were often made, to calibrate the magnet so that field values could be

known for data taken with sample holder SP-1, which lacked an n.m.r.

specimen. It was found that the direction of field sweep again had a

slight effect on the field-current calibration of the magnet. For a

"z-gradient" setting of 0.0 and a "curvature" setting of 5.95 (a compen-

sating current of 0.160 ampere), the magnetic field was found to be re-

lated to the current by

$$H \text{ (kG)} = 3.046 \text{ I (amps)} + \begin{pmatrix} .440 \text{ (ramping up)} \\ .475 \text{ (ramping down)} \end{pmatrix} \pm 0.025 \text{ kG.} \quad (15.)$$

For these same magnet power supply settings, the field at the dHvA

sample was 16 ± 4 G less than that sensed by the n.m.r. specimen 5/8

inch away; this less-than-optimum homogeneity was used because of its

reproducibility.

A block diagram of the experimental arrangement is shown in Figure

6. The modulation frequency was provided by the oscillator section of

an Optimation AC-15 power oscillator, which was typically set to 77.3 Hz

to match the band-reject filter in the pickup circuit. In order to

provide a constant value for the argument of the Bessel function in

Equation (12.), the amplitude of the modulation current was adjusted to

be proportional to the square of the current through the superconducting

solenoid, by means of the circuit shown in Figure 7. Using a self-

balancing potentiometer approach, the servo motor drove the first

potentiometer to balance the voltage developed by the magnet power

supply current as it passed through a 0.008-ohm standard resistor in

series with the main solenoid. The amplitude of the a.c. signal picked

off the second ganged potentiometer was then proportional to the magnetic

FIGURE 6: The experimental arrangement for the field modulation technique, depicting the n.m.r. circuit to monitor the field and the digital circuit to record the dHvA data.
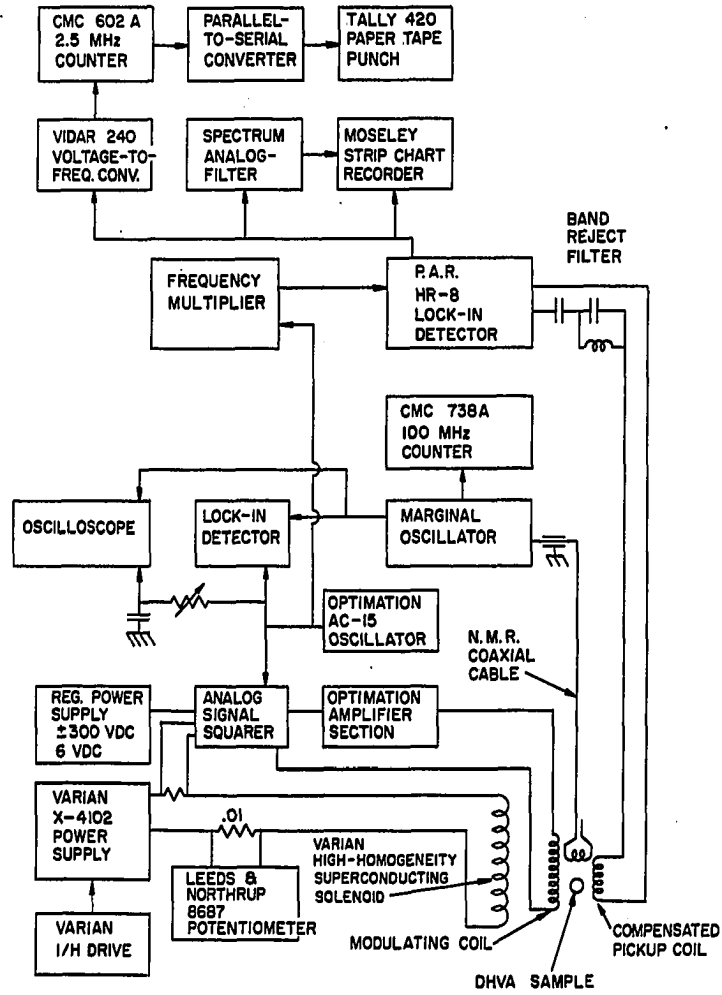
FIGURE 7: The analog circuit used to vary the amplitude of the
           alternating current to the modulation coil in proportion
           to the square of the direct current to the superconducting
           solenoid. A sketch demonstrating the current-control
           principle is inset in the lower left corner.
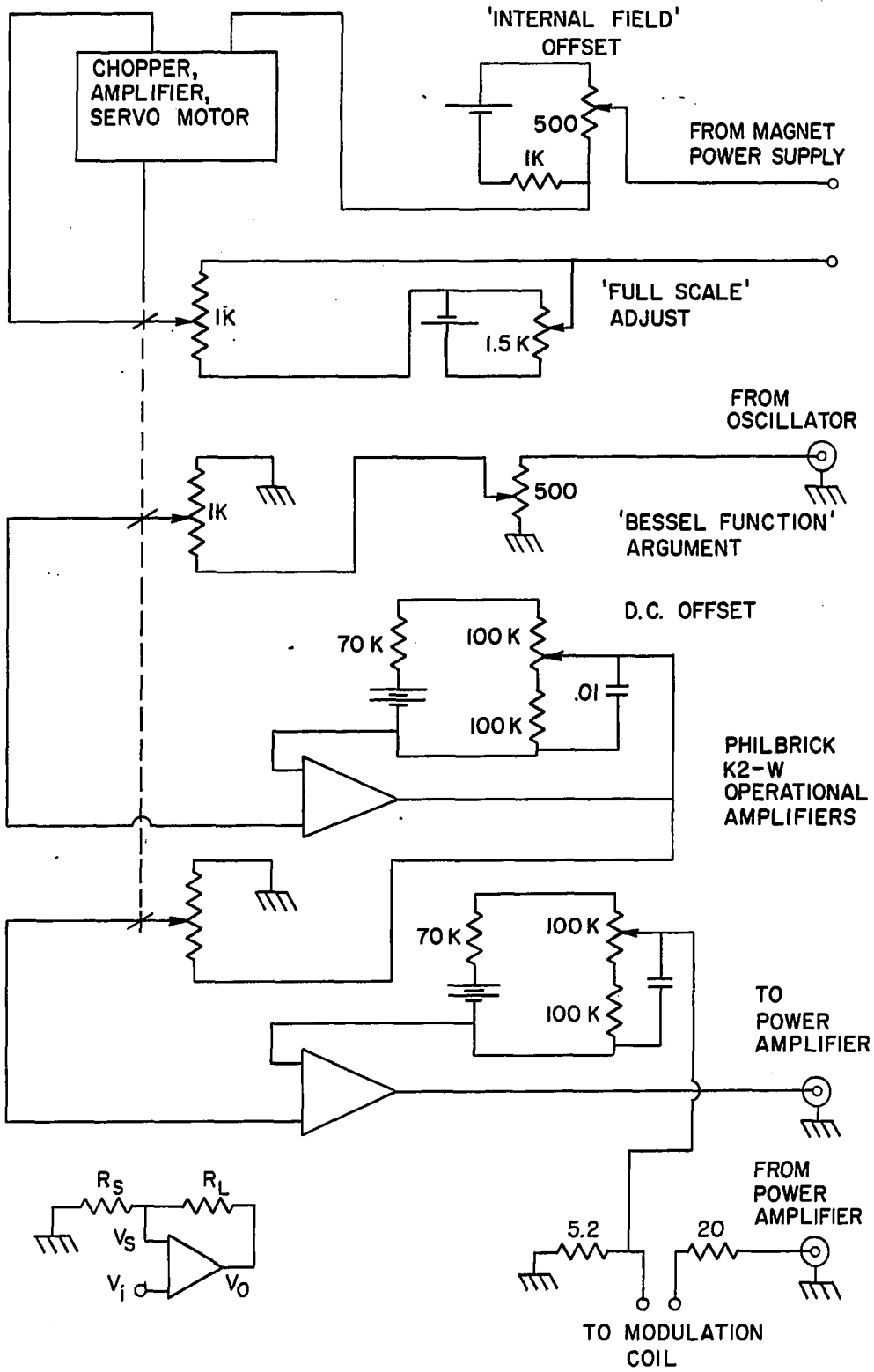
field. After being isolated by a Philbrick K-2W operational amplifier,

this a.c. signal was fed into the last potentiometer, so that the

amplitude of the signal detected by the second operational amplifier

was proportional to the square of the field. This amplifier drove the

power amplifier section of the Optimation oscillator. One lead of the

modulating coil was connected to the output of the Optimation amplifier,

and the other end of the coil was connected to the second input of the

operational amplifier and thence through a 5-watt, 5.2-ohm resistor to

ground, forming a closed loop. Current control was achieved because of

the high input impedance and amplification of the operational amplifier.

With reference to the inset of Figure 7, we have

$$V_o = A(V_i - V_s) \quad , \tag{16.}$$

and

$$V_s = V_o - i_L R_L = i_s R_s \quad , \tag{17.}$$

so that

$$AV_i - (1 + A)V_s = i_L R_L \quad . \tag{18.}$$

For A large,

$$V_i - V_s \doteq \frac{i_L R_L}{A} \doteq 0 \quad , \tag{19.}$$

meaning that

$$i_L = i_s = V_i/R_s \quad , \tag{20.}$$

i.e., i_L is controlled by V_i .

Successful use of this circuit depended on both sides of the modulation coil being ungrounded, as well as on a low inductive reactance and on d.c. coupling to prevent any spurious oscillations. It is felt that any fluctuations of the Bessel-function argument $2\pi F_r h_{eff}/H_o^2$ were due to deviation from linearity of the potentiometer. Beckman 0.5% Helipots were used, but it is planned to replace these with more precise potentiometers in the future.

The modulating field h (~100 G) superimposed on the field from the superconducting solenoid (~ 50 kG) was also used for the n.m.r. calibration of this main field. The n.m.r. signal was displayed as the vertical trace of an oscilloscope, while the horizontal sweep was derived from the Optimation oscillator. The latter signal was phase-shifted to allow accurate centering of the Al^{27} resonance, to a precision of 1 gauss. A Princeton Applied Research (P.A.R.) JB-5 amplifier was sometimes used, to detect the n.m.r. signal under noisier conditions.

The dHvA signal induced in the pickup coil was fed to the Type B 100:1 preamplifier of a P.A.R. HR-8 lock-in amplifier, which used a suitable multiple $n\omega$ of the modulation frequency ω as the reference; the harmonic number n determined the order of the Bessel function in Equation (12.). This signal was displayed as one trace of a Hewlett-Packard Moseley 7100-B two-pen stripchart recorder, and was also recorded by the digital recording apparatus described below.

The digital circuitry, which enabled the dHvA signal to be recorded

on punched paper tape for computer analysis of the frequencies, consisted

essentially of a timer, digital voltmeter, parallel-to-serial converter,

and paper tape punch. The 0 - $\pm$10 V output of the lock-in amplifier

was presented to a Vidar 240 voltage-to-frequency converter, which con-

verted it to a 0 - 100 kHz signal with sign bit, with 0.1% linearity.

This frequency was determined by a C.M.C. 602A frequency counter, which

transmitted the three most significant digits to the parallel-to-serial

conversion network shown in Figure 8.

The timing circuit is shown at the top of this figure. The input

timing frequency was usually derived from the 60-Hz line, although

provision was made for an external oscillator. The sine-wave signal was

converted to a rectangular wave, differentiated, and half-wave rectified

to produce a 60-Hz pulse, which triggered a sequence of flip-flops for

a total timing cycle of 64/60 seconds. The "start" and "stop" flip-

flops were triggered pushbutton switches, and the "stop" signal was

anded with pulse #63 of the timing cycle, to permit the entire 3-digit

number to be recorded before the punch was stopped. A 7-ms delay

"enable-decode" (E.D.) pulse allowed all flip-flops to stabilize before

they could be read, leaving 10 ms of each 1/60 sec (=17 ms) pulse interval

for switching. The "convert" circuit controlled a transistor gate

switch in the frequency counter, turning it on at count #1 and off at

count #3, permitting a gate time which was more than adequate.

The 1-2-4-8 binary-digit (BCD) output from the counter was buffered

by an interface circuit to avoid overloading and erroneous readings.

Gate 1 was on during counts #30 and #31, and was anded with the hundreds

FIGURE 8: A schematic diagram of the parallel-to-serial converter used in digital recording of the dHvA data.
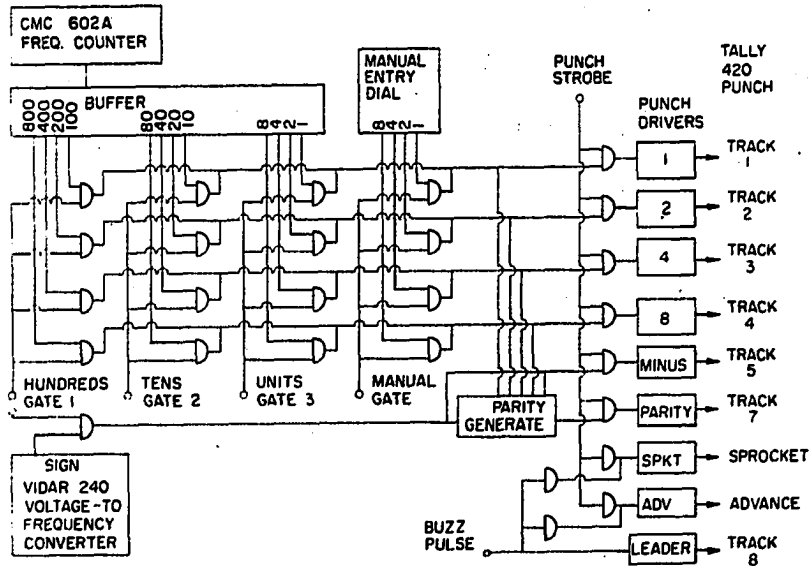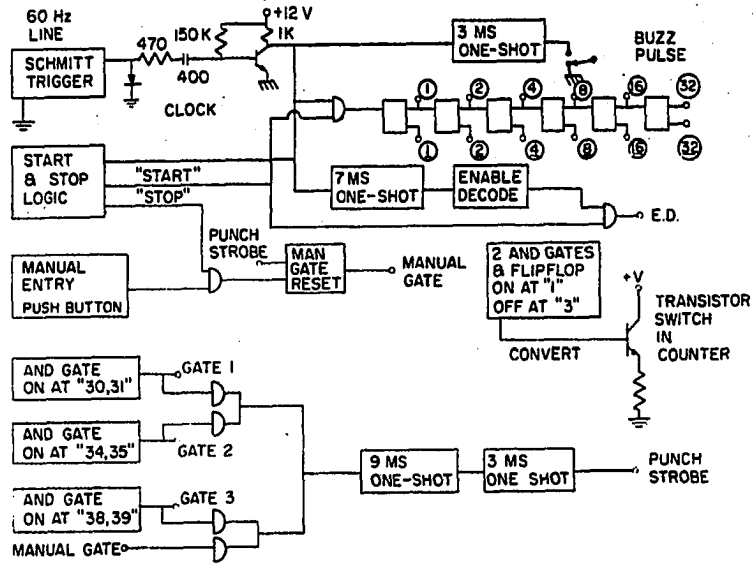
decade and the sign bit from the voltage-to-frequency converter. This
activated the punch drivers, in conjunction with the punch strobe which
was turned on 10 ms later and lasted for 3 ms, as required by the Tally
420 tape punch. The parity generation circuit operated in this 10 ms
interval, to add the parity punch as a check on operation of the Tally
punch. The intermediate parity logic bit N was generated by

$$N = (2.\overline{1} + 1.\overline{2}) \cdot \overline{(8.\overline{4} + 4.\overline{8})} + (2 \cdot \overline{1} + 1.\overline{2}) \cdot \overline{(8.\overline{4} + 4.\overline{8})} \quad , \quad (21.)$$

which was "on" if an odd number of the BCD bits were "on". The final
parity bit P was then generated by combination with the minus sign
bit S, through the relation

$$P = \overline{N} \cdot \overline{S} + N \cdot S \quad , \qquad (22.)$$

which in normal operation produced an odd number of punches per frame
of the tape.

The next most significant number was punched when Gate 2 was on
during counts #34 and #35. Finally, Gate 3 was on during counts #38
and #39, and was anded with the units decade. Additional switching and
gating was provided for manual entry of numbers, and this circuit was
reset by the punch strobe to prevent multiple punching of a desired
number. The buzz pulse circuit provided 60-Hz leader punches on track 8
of the tape, as well as a "stop" signal to prevent data collection during
leader generation. In a similar separation of function, the manual

punch was _anded_ with the "stop" signal to prevent manual entry during the data-taking cycle.

The data readings recorded by the above circuitry ranged in value from +999 to -999, with the minus sign indicated by an extra punch concurrent with the most significant figure of the three-digit number. The sign was extracted in the analysis program by the "MESS" subroutine written by G. Covert of the Computation Center (see Appendix I).

The parallel-to-serial converter was constructed from 18 Scientific Data Systems (S.D.S.) card modules and was driven by an S.D.S. PX-10 +25, +8, -25 VDC heavy-duty power supply. The circuit has performed well, save for an occasional parity violation, but the circuit can be tripped to "stop" by large line transients. If an external oscillator were used to drive the timing cycle, the upper limit of conversion speed would be three complete cycles per second, as determined by the delay times involved and by the gate time of the frequency counter.

The dHvA signal from the lock-in amplifier was also sent to a Spectrum LH-42D 0.02 Hz-2 kHz analog filter, incorporating two high/low stages, with an attenuation of 42 db/octave per stage. This filter was sometimes used for additional discrimination of dHvA frequencies, as mentioned in the preceding chapter. However, the 1/H drive of the magnet power supply was rarely used after the digital recording system was put into operation, because the drive ramped solenoid current, rather than field, in proportion to 1/time. The static current-field relation (as in Equation (15.)) also had an additive constant due to "trapped flux", and the field could not be ramped precisely as 1/time, thereby making

digital analysis more difficult for data taken in this manner. The output of the filter operating in the high-pass mode was nonetheless recorded on the analog strip chart recorder, to serve as an eventual check on the digital analysis of the high-frequency dHvA data.

In the recording of the fieldsweep data, allowance was made for a 4-sec lag in the initial response between the power supply and solenoid, presumably due to eddy currents in the spool. Use of the n.m.r. signal circumvented this problem, and the "start" or "stop" button was pushed as the center of the resonance was observed during field ramps. Figure 9 shows a typical field sweep for thorium, where resonances at 47.978 MHz (43.194 kG) and at 63.565 MHz (57.220 kG) were used as signals for the beginning and end of the digitized data set. The marginal oscillator was stable to 0.0001 MHz during the 1 second gate time of the C.M.C. 738A 100 MHz direct-reading frequency counter used, allowing a precise determination of the fields.

Power supply linearity of ramp was better than 0.1%, and it had a negligible effect on the linewidth of the frequency spectrum produced by the analysis program. Towards the end of the data-gathering phase of the experiment, the slip clutch on the ramping motor caused an occasional pause in the upward ramp of the power supply. When analyzed by the computer, such data were found to produce dHvA frequencies which were ~ 1% too high; however, the pause was clearly noticeable on the analog data, and could be taken into account.

To conclude this section on the experimental procedure, it might be well to review all of the situations in which the term "frequency"

FIGURE 9: dHvA oscillations arising from a typical field sweep using the worm-gear
           sample holder, with the field direction set at 57° from [100] in the (110)
           plane. The digital recording apparatus was turned on at the first n.m.r.
           marker and turned off at the second. The gap AB denotes the time interval
           during which the lock-in amplifier was disconnected and the marginal
           oscillator was tuned to the second frequency.

INCREASING TIME
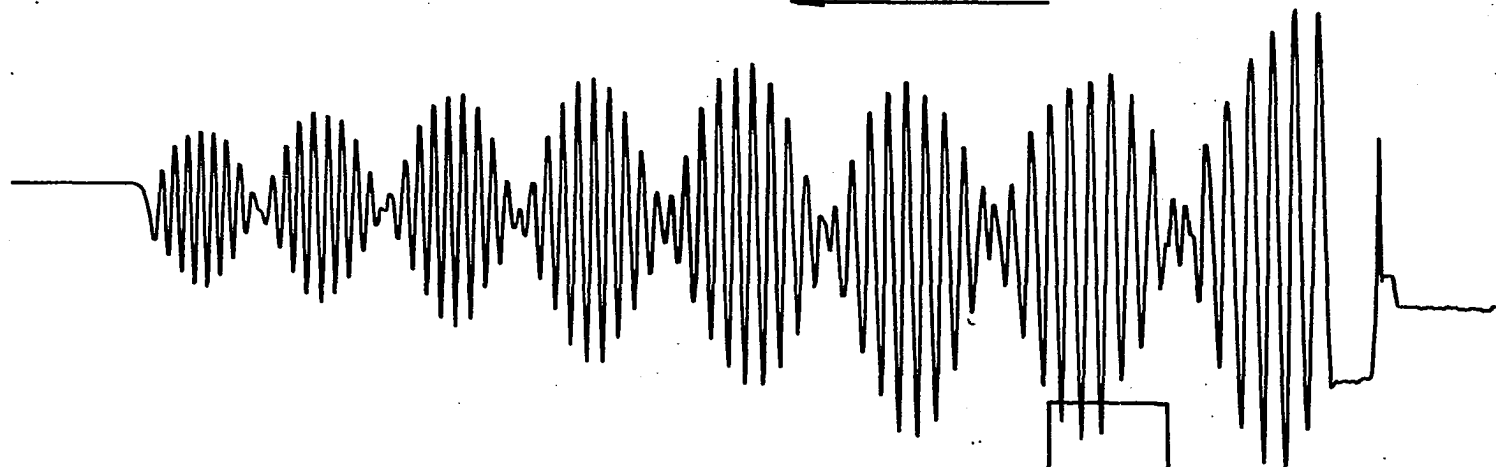
47.978 MHz
(43.194 KOe)

B

A
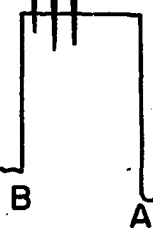
63.565 MHz
(57.220 KOe)

45

was used:

1.) The dHvA frequency F_r is associated with a particular extremal cross-sectional area $\mathcal{A}_r$ of the Fermi surface, in a plane normal to the direction of the field. Several cross-sectional extremal areas may exist if the Fermi surface is complex, leading to complicated dHvA waveforms. The dHvA oscillations are expressed as $\sin\left(\dfrac{2\pi F}{H_o}r\right) = \sin\left(\dfrac{2\pi F}{H_o^2}r\dot{H}_o\, t\right)$,

leading to the expression for the time-frequency of the dHvA oscillations as $F_r \dot{H}_o/H_o^2$. For example, we might have $F_r = 10$ MG, $\dot{H}_o = 20$ G/sec, and $H_o \approx 50$ kG, in which case the time-frequency would be ~ 0.08 Hz.

2.) The modulation frequency ω was in the 30-100 Hz range for this experiment. The second or fourth harmonic of ω was used as the reference frequency to the lock-in amplifier, to permit exploitation of the behavior of J_2 or J_4.

3.) The line frequency of 60 Hz was used as the timing pulse for the digital recording circuit.

4.) An intermediate step of the digital recording circuit used a voltage-to-frequency converter, which operated in the audio-frequency range.

5.) The n.m.r. frequency was proportional to the main field; for an applied field of 50.000 kG, the n.m.r. frequency was 55.556 MHz. For a

fixed n.m.r. frequency, the n.m.r. absorption was detected by the field modulation method, with the reference frequency set to the fundamental, ω .

3.2 Digital Analysis of the Data

A modification of a program developed by Panousis (1967) was used for computer analysis of the data, and an annotated listing is displayed in Appendix I. This program interpolated the data (which were originally recorded at equal increments of time) to give points at equal increments in $1/H$, and then treated the data as a driving function for a numerical analog to an electronic filter with $Q \sim 10$. The filter response was computed for each discrete dHvA "pass-frequency" in a desired range, with the increment between frequencies being set by the resolution needed. The results of this initial filtering were then analyzed by a periodogram technique (Girvan, Gold, and Phillips, 1968) to improve the discrimination. This program may be thought of as numerically reproducing the behavior of a multi-phase lock-in amplifier, which consists of a tuned amplifier followed by a correlation detector locked to an external reference frequency.

Panousis' program was capable of resolving frequencies to better than 1%, and of discriminating between comparatively low-level signals and noise. It did have some limitations, however, one handicap being the large amount of computer core space (128 K or more) which was required. For instance, a third of this core space was taken up by the interpolated input data, which consisted of a sequence of the 10,000 or more points which were required for the periodogram analysis. If we consider the

dominant frequency in thorium with F = 10 MG, we find about 83 cycles for

the field range between 40 kG and 60 kG, and since 100 points per cycle

were required for 1% resolution, this required a sequence of 8300 inter-

polated points. In the analysis of the higher frequencies (F ≈ 20 MG),

a sequence length of 10,000 was retained, and a degradation of the re-

solution to about 2% was in fact observed. Resolution could be improved

by limiting the field range, as was done by the use of the program variable

"NSTRT", which specified the number of low-field data points to be dis-

regarded. The exact positions of the maxima in the frequency spectrum

were found from a second-order fit to the three highest intensity values

in the neighborhood of each maximum, thereby compensating in part for the

inaccuracies caused by the discrete frequency increments of the filter.

The initial reason for choosing the filter-periodogram analysis

rather than conventional Fourier analysis was for reasons of economy

in machine time; the equations involved in the former do not require the

comparatively time-consuming computation of sines and cosines in the

latter. Recently, however, Cooley and Tukey (1965) and others have

developed methods of streamlining Fourier transforms into highly-efficient

algorithms which are suitable for digital computers and which result in

enormous savings of time if the number N of data points is large and if

$N = 2^m$, where m is an integer. This so-called "fast Fourier transform"

is now available as a standard IBM subroutine "RHARM" and a program

exploiting "RHARM" for dHvA frequency analysis is given in Appendix II.

In comparison to the filter-periodogram approach, the fast Fourier trans-

form technique was found to reduce the analysis time for a typical dHvA

data set by a factor of 20.

In practice, however, the effective resolution of the fast Fourier transform was more limited than that of the filter-periodogram by the finite size of the data set, as can be seen from the following considerations. We write the incremental expression for a Fourier transform as

$$X(J) = (1/2)A_0 + \sum_{K=1}^{N} [A(K)\cos(\pi JK/N) + B(K)\sin(\pi JK/N)] \quad , \quad (23.)$$

where N is half of the number of points in the J-set, and X(J) is the amplitude of each input data point; the fast Fourier transform technique requires that $N = 2^{m-1}$. The index J on the input data runs from 0 to $2N-1$, and if we let G = 1/H (i.e., reciprocal field), the incremental sequence G(J) of reciprocal field points corresponding to the interpolated data set X(J) can be generated by $G(J) = G_1 + \dfrac{G_2 - G_1}{2N} J$, where the end points G_2 and G_1 correspond to the fields H_2 and H_1, which have been measured (e.g., by n.m.r.). We note that there are 2N points in the X(J) set, N+1 points in the A(K) set (K = 0, 1, 2, ..., N), and N-1 points in the B(K) set (K = 1, 2, ..., N-1) since B(N) is undefined, being the coefficient of $\sin(\pi JN/N) = 0$. In our case, the usual expansion (Equation (8.)) in terms of the dHvA frequencies F(K) would be written as

$$X(J) = \sum_{F} A(F) \sin(2\pi FG(J) + \phi(F)) \quad . \tag{24.}$$

If we set

$$F(K) = K/(G_2 - G_1) , \tag{25.}$$

the argument of the sine becomes (neglecting constant phase factors)

$$2\pi \times \frac{K}{G_2 - G_1} \times \frac{G_2 - G_1}{2N} \times J = \pi JK/N \quad ,$$

as required for Equation (22.)). It is therefore seen that the frequency resolution ΔF will be $1/(G_2 - G_1)$, and in the optimum case with $H_1 = 60$ kG and $H_2 = 40$ kG, the resolution can be calculated to be $H_1 H_2/(H_1 - H_2) = 0.12$ MG, i.e., 1.2% for the dominant terms ($F \approx 10$ MG). However, the resolution improved with frequency (in contrast to the Panousis program) and was 1% or less for the higher frequencies ($F \approx 20$ MG) observed in thorium.

On the other hand, the resolution was found to be too "sharp" when RHARM was used to analyze higher frequencies, since the Fourier trans- form assumed a constant amplitude $A(F)$ for each frequency component, whereas the dHvA amplitude in fact increases with field. This varying amplitude resulted in a splitting of the central peak in the frequency spectrum found by the Fourier analysis. One could take the mean value of the positions of the two peaks, which would give the proper maxima for a spectrum in which these maxima were well separated and significantly above the noise level. However, the principal reason for using digital analysis was to resolve dHvA terms for which the frequencies may be close together or the intensities may be low; for such terms, the splitting was a disadvantage.

However, no such splitting was observed in the filter-periodogram program, since it summed amplitudes at similar phase points and made no assumptions about the constancy of the amplitude. In another sense,

however, the field dependence of the amplitude did affect the periodogram, since larger amplitudes (which occured at higher fields) would contribute more to the summations than would the lower amplitudes at lower fields. However, the interpolated data points were more reliable at the high-field end, since the original input data set was closely spaced in reciprocal field for higher values of the field; the time frequency of the dHvA oscillations, being proportional to $\dot{H}H^{-2}$, decreased with increasing field H, leading more sampled points per cycle at higher field strengths. As far as this experiment is concerned, the absence of splitting at higher frequencies and the higher resolution attainable at lower frequencies led us to prefer the filter-periodogram analysis technique to the fast-Fourier-transform method.

IV. EXPERIMENTAL RESULTS

4.1 dHvA Frequency Data

An overall plot of the experimentally observed frequency branches is presented in Figure 10 for the (110) and (100) planes. With the exception of a new branch $F_{11} \approx 2.5$ MG, most of the data fall into two relatively narrow bands of 9.5-14 MG and 19-25 MG, as found earlier by Thorsen, Joseph, and Valby (1967). In order to facilitate the discussion below, the actual data points for the intermediate frequency band are graphed in greater detail in Figure 11. Open symbols in this figure represent field-sweep data characterized either by low signal levels (comparable with or less than the periodogram noise threshold) or by large (>1%) scatter between points determined from successive field sweeps. The smaller symbols represent relative frequency variations determined by the rotation technique; this method was particularly helpful in delineating the frequency branches in the (110) plane. Because of the previously mentioned orientation problems which resulted in a pronounced splitting in the observed frequencies, data taken with the wire-driven sample holder SP-1 were not plotted for the (110) plane.

We consider first the dominant branch F_1, which had a signal level near [110] about 3-4 times larger than elsewhere in the plane. This increase in signal at [110] is illustrated by the constant-field rotation sweep data for the (100) plane in Figure 12, using a crystal mounted in the wire-driven sample holder. The frequency variation $F_1(\theta)$ in the (110) plane (Figure 11) was found to increase as $1/\cos \theta$ near [110], where θ is the azimuthal angle as measured from this orientation. For

FIGURE 10: The angular dependence of the dHvA frequencies observed
in the present experiment, for both the (110) and (100)
planes.
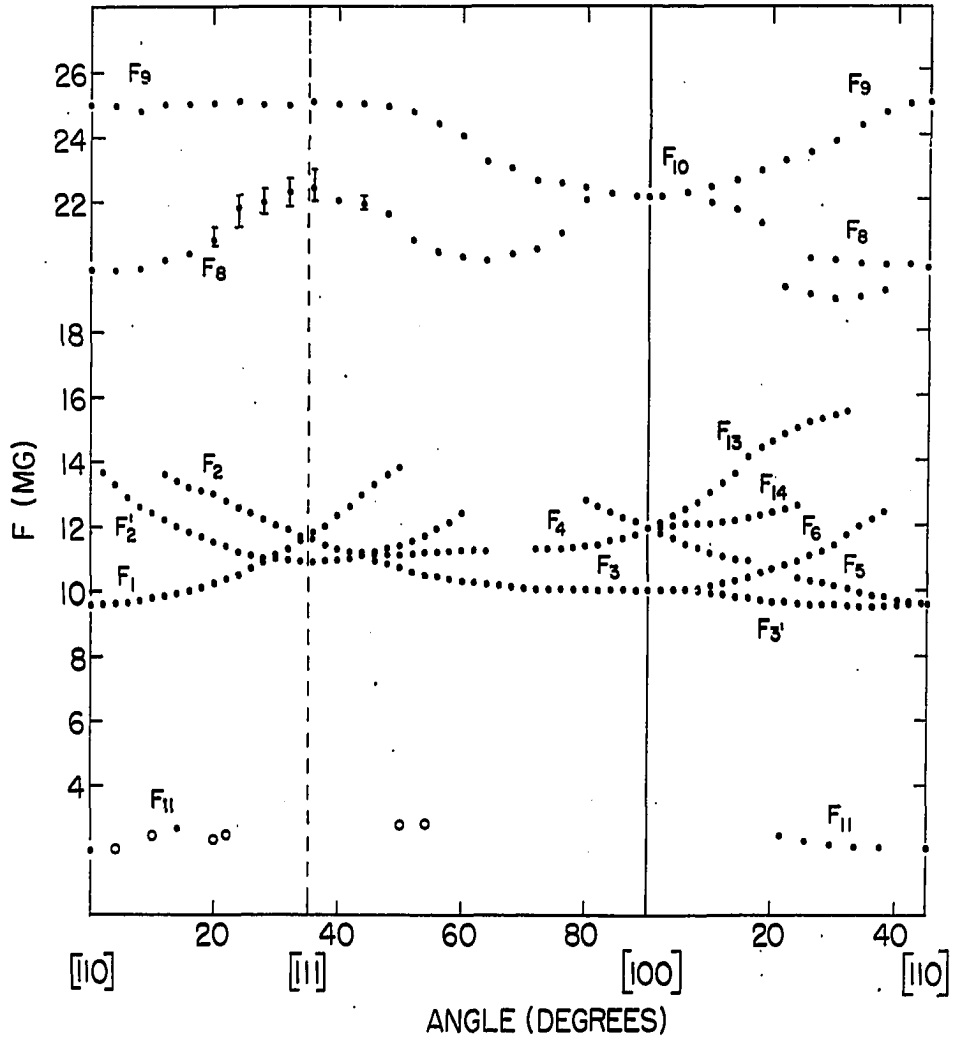
FIGURE 11: The experimental data in detail for the intermediate dHvA frequencies. The
larger symbols represent points taken by field sweeps using:

1.)   the wire-driven sample holder SP-1 with a fixed pickup coil
(triangles), or

2.)   the worm-gear sample holder SP-2 having the crystal mounted with
its [110] direction along the axis of the pickup coil (squares), or

3.)   the worm-gear sample holder SP-2 having the crystal mounted with
its [100] direction along the axis of the pickup coil (circles).

Open symbols signify data characterized either by large (> 1%) scatter
between points determined from successive field sweeps or by signal
levels comparable with or less than the periodogram noise threshold. The
smaller symbols indicate relative frequency points obtained from direct
study of rotation sweeps made at constant fields.

THORIUM (110) PLANE   (100) PLANE
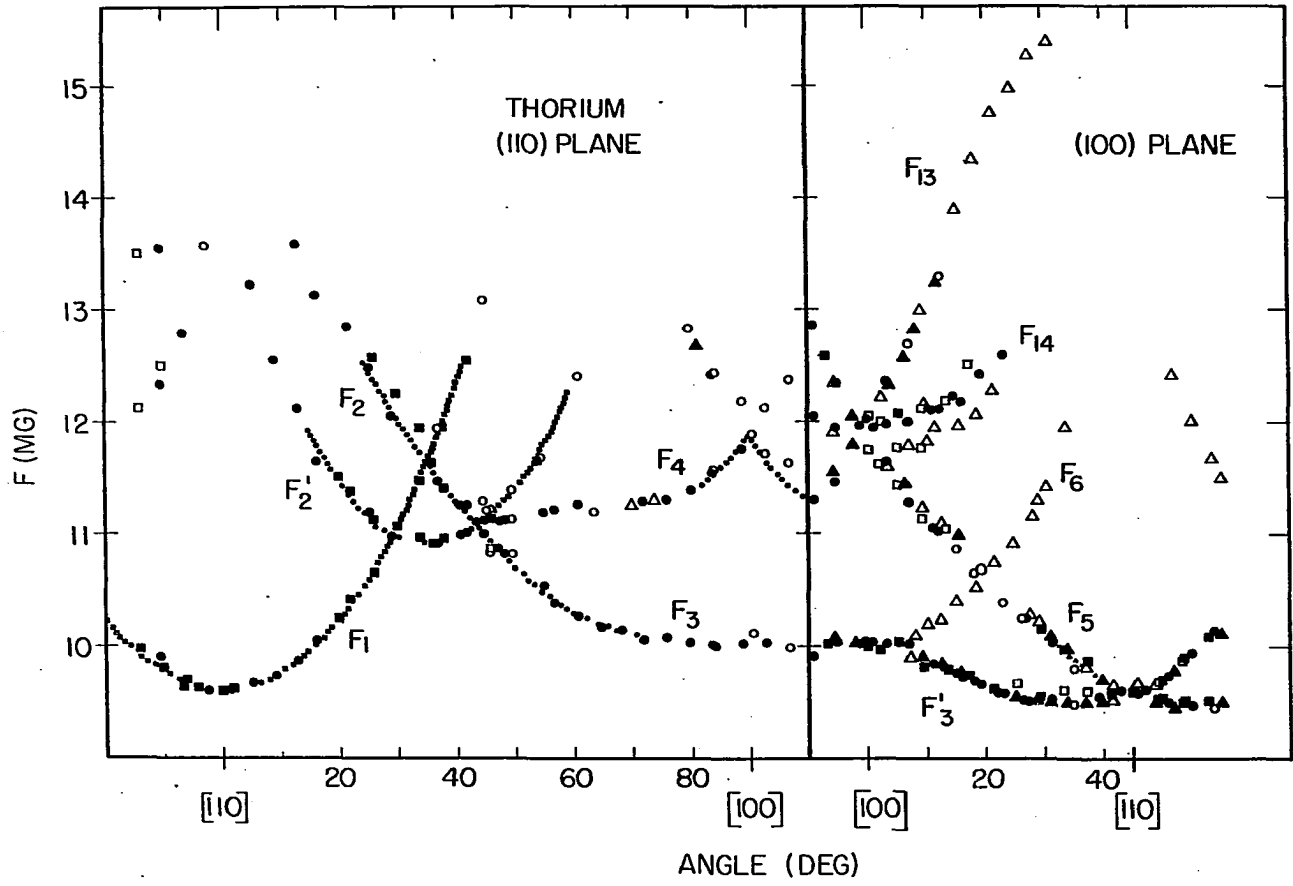
FIGURE 12: A reproduction of data taken by the modulated-field
method for constant-field rotation of a crystal
mounted in the wire-driven sample holder SP-1 and
rotated in the (001) plane. An oscillation is
recorded each time that a frequency branch changes
with angle by the amount H (i.e., $\Delta F_r = H$). The
frequency branch F_c is seen to vary at a constant
rate through the symmetry directions [100] and
[110], and to decrease in amplitude in part of the
intervening range.

H = 55.00 kG

[100]

[110]

H = 50.00 kG
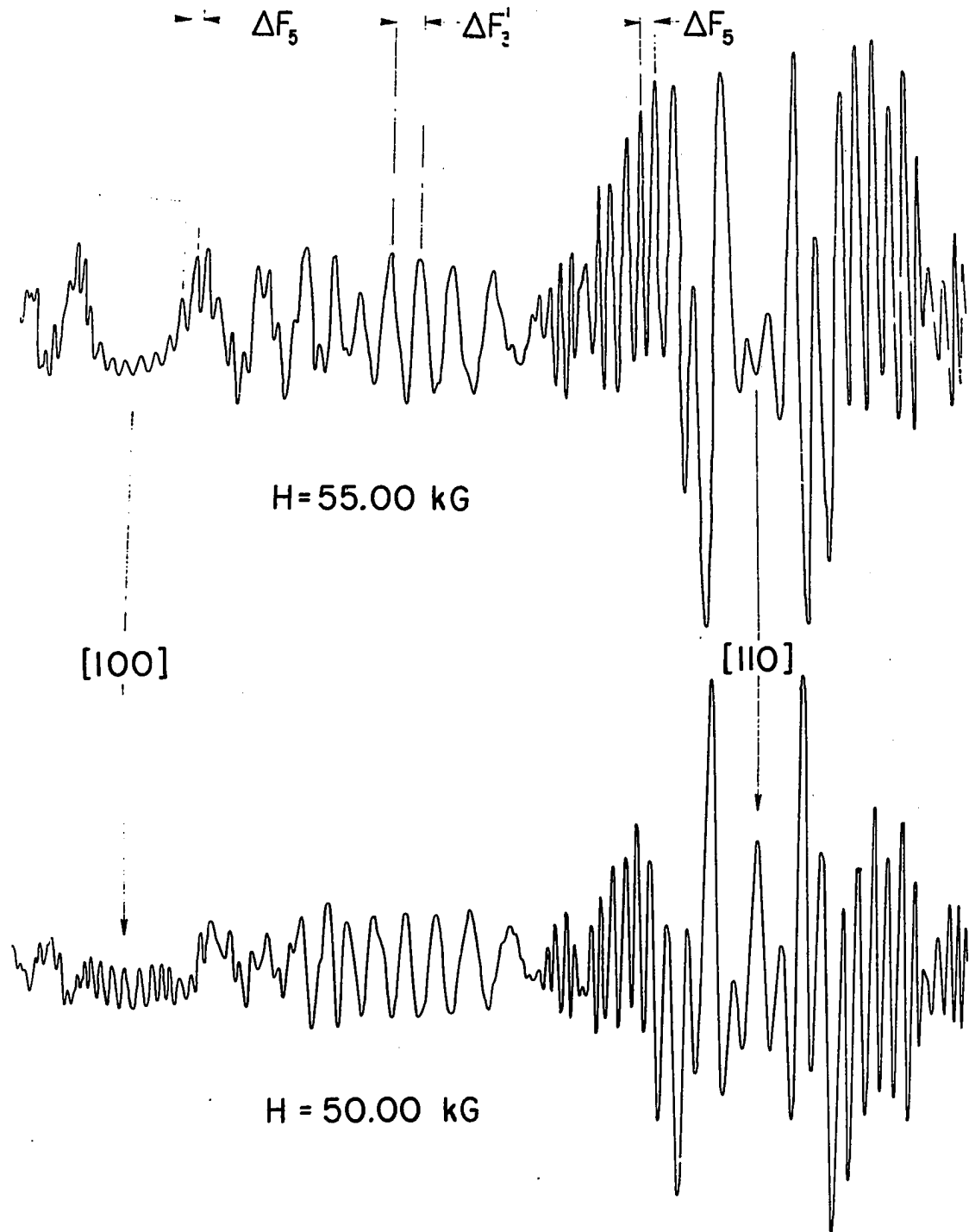
$\theta > 30^\circ$, $F_1(\theta)$ increased less rapidly than $1/\cos \theta$, and at $\theta = 42^\circ$ the difference between $F_1(0)/\cos \theta$ and $F_1(\theta)$ was roughly 0.3 MG or 2.5%, a difference greater than the experimental error of 1%.

In contrast to the single branch F_2 observed by Thorsen et al. (see Figure 1), we have been able to separate F_2 into two terms, F_2' and F_2, which could be followed to within 3° and 13°, respectively, of [110]. The branch F_2' exhibits a minimum at [111] and increases in frequency faster than the inverse of the cosine of the angle as measured from [111]; this suggests that the relevant portion of the Fermi surface is hyperboloidal in form, and dumbbell-shaped if it happens to be a closed sheet. A dumbbell-shaped surface with axis along [111] would in turn require a frequency branch symmetric about [111] and higher than F_2', this second branch would arise from the maximum non-central areas of cross-section, whereas F_2' would be due to the central minimum. (See right side of Figure 13 for a sketch of the expected surface.) Such a branch of higher frequency would be expected to increase at a slower rate than $1/\cos \theta$ and at a certain orientation the two branches should join; see Pippard (1965) for a more detailed discussion of this behavior[*]. Unfortunately, the observed amplitude of branch F_2' became vanishingly small at $\pm 32^\circ$ from [111], and no coalescing with a branch of higher frequency had been observed in this small angular interval.

---

[*]In the special case of ferromagnetic nickel (Hodges, Stone, and Gold, 1967), a frequency-branch variation more rapid than $1/\cos \theta$ has been attributed instead to orientation-dependent ferromagnetic spin-orbit coupling and a resulting change in Fermi-surface dimensions with direction of field.

FIGURE 13: The variation of the central extremum of cross-sectional area
with change of field direction, for various types of closed
Fermi surfaces. An increase in $\mathscr{A}_0$ with angle θ at a more
rapid rate than $1/\cos \theta$ implies the existence of a non-central
maximum area (indicated by the arrow).
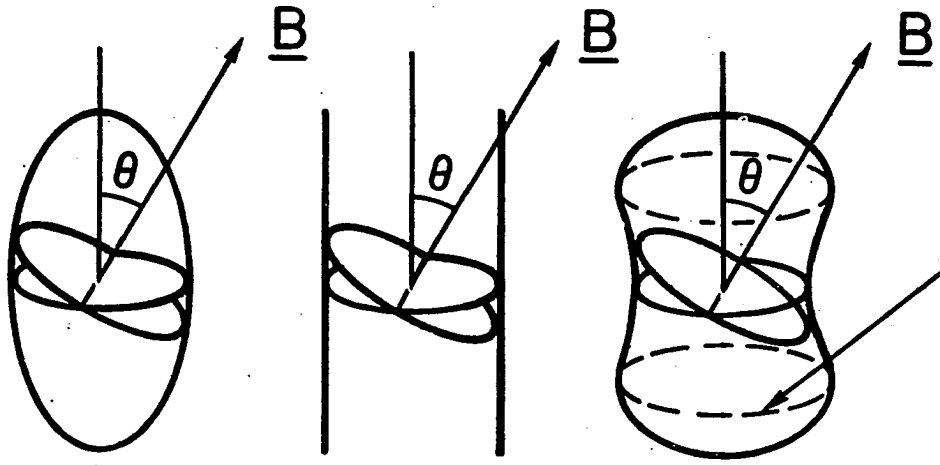
$$\mathscr{A}_\theta < \frac{\mathscr{A}_0}{\cos \theta} \qquad \mathscr{A}_\theta = \frac{\mathscr{A}_0}{\cos \theta} \qquad \mathscr{A}_\theta > \frac{\mathscr{A}_0}{\cos \theta}$$

FIGURE 14: A static-field rotation sweep for the $(1\bar{1}0)$ plane in thorium. The variation of the F_4 branch appears to be constant with rotation through $[001]$ whereas the variation of F_3 decreases in a manner characteristic of a turning point. The branch F_2' is symmetric about its turning point at $[111]$, and the variations F_2' and F_2 diminish in amplitude as $[110]$ is approached. The relative amplitude of the frequency branch F_1 near $[110]$ is decreased because of attenuation by the factor $\partial F/\partial\theta$; the crystal was mounted in the worm-gear sample holder with the $[100]$ direction along the axis of the rotating pickup coil. (This arrangement can be demonstrated in Figure 3 (b.) by placing $\hat{\underline{\mu}}$ along k_x and setting $\theta_o \gtrsim 0^o$.)

ΔF_4 ΔF_3 ΔF_2 $\Delta F_2'$ ΔF_1

H = 56.99 kG

[OOI]   [III]   [IIO]

H = 50.00 kG

63
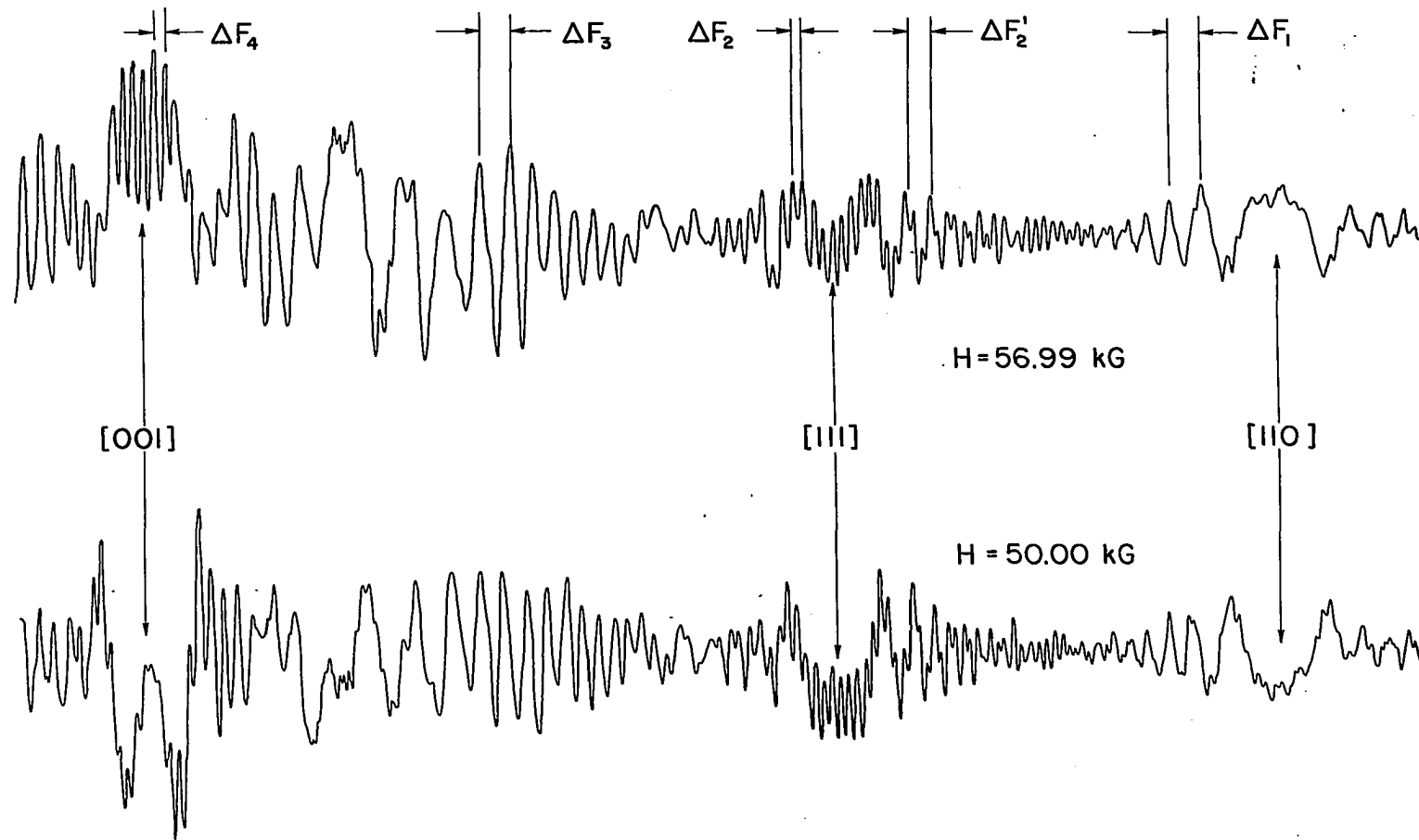
The other frequency branch F_2 was followed from its point of appearance at 13° from [110], and was found to cross F_1 at [111] (see Figure 11). At $\theta \approx 42^o$, F_2 appeared to split into two components, labelled F_3 and F_4. The upper branch F_4 became difficult to follow over the angular range 64° - 70°, and it is felt the amplitude of this term may have been reduced because of a low value of the spin-splitting factor $\cos(\frac{\pi g m^*}{2m_o})$ (i.e., $m^* \approx \frac{1}{2}m_o$ and $g \approx 2$). Near [100], the lower branch F_3 was nearly flat, while F_4 was found to increase in frequency as it approached [100]; F_4 appeared to have a crossing point at [100], although the oscillations corresponding to this frequency were of low intensity.

Further evidence for a crossing-point for the frequency branch F_4 at [100] can be seen from the constant-field rotation curve in the (110) plane shown in Figure 14; this tracing clearly illustrates the continuing change of F_4 with rotation through [100], rather than the decreasing rate of change characteristic of a turning point. Such a turning point for the branch F_2' at [111] is evident in this rotation curve, as well as the decrease in amplitude of the rapidly-varying frequency branches F_2 and F_2' as [110] is approached. This rotation curve was generated with the worm-gear holder having the [100] direction of the crystal along the coil axis; the normally dominant term F_1 was reduced in amplitude relative to F_2 or F_2', since $\partial F/\partial \theta$ was negative for the term F_1.

Turning now to the (100)-plane data (Figure 11) for the intermediate frequencies, the most striking feature is that three branches appear to meet at [100], with a common frequency of 11.9 MG. The branch F_{13} was found to cross the branch F_5, while the term F_{14} appeared to have a

FIGURE 15: The observed data points for the dHvA frequency band of 19-25 MG, using the same symbols as in Figure 11. The 19-MG frequency branch in the (100) plane is evidently a harmonic of the 9.5-MG branch in the intermediate-frequency band.

THORIUM (110) PLANE / THORIUM (100) PLANE
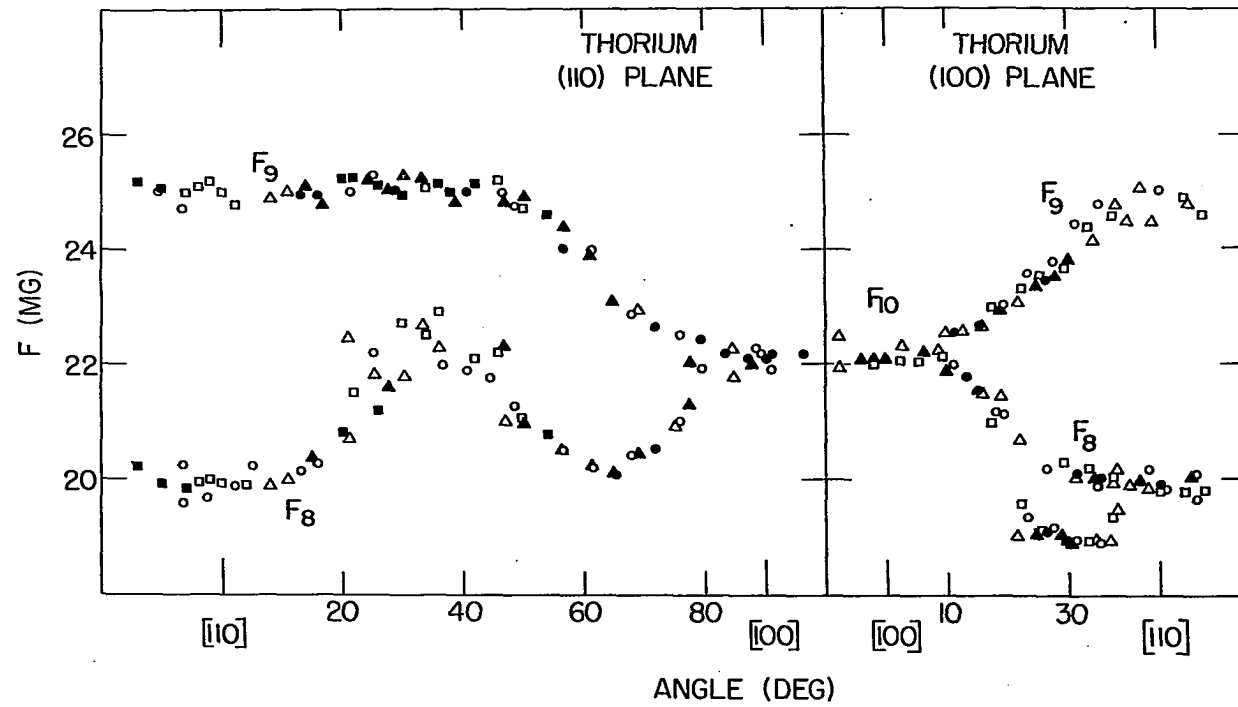
turning point at [100]; F_{14} could be followed only over a limited range of $\pm 23°$ from [100]. The branch F_5 diminished in amplitude in the $15° - 25°$ range, as can be seen from the (100)-plane rotation sweep reproduced in Figure 12. The term with lowest frequency at [100], F_3, appeared to split into branches F_3' and F_6 at $7°$ from [100]. The lower-frequency branch F_3' decreased in value from 10.0 MG to a minimum of 9.50MG at $11° \pm 2°$ from [110] and then increased to 9.58 MG at [110], where it was observed to cross F_5. The higher-frequency branch F_6 was observable only from field sweeps taken with the wire-driven sample holder SP-1.

Considering now the higher-frequency band in the range 19.5-25 MG, the general behavior of our results, as shown in greater detail in Figure 15, does not differ significantly from that found by Thorsen et al.. The possible presence of harmonics may have been responsible for the scatter of some of the data points near [111] in the (110)-plane; however, a careful check of the rest of the data for this plane indicates that neither of the frequency branches shown is a harmonic of the previously-considered lower ones. The upper frequency branch F_9 was nearly flat over a wide range [110] with a value of 24.8 MG; for angles greater than $48°$, F_9 appeared to decrease rapidly in frequency to the minimum value F_{10} of 22.1 MG at [100]. The lower-frequency branch F_8 was the weaker term, with a frequency of 19.9 MG at [110], and became especially difficult to follow near [111].

Turning next to the data for the (100) plane, the branches varied smoothly in frequency toward the values at [110], and we note that some of the points in the branch F_8 may be due to the harmonics of the 9.5 MG

and 10 MG frequencies. A diligent search for still higher frequencies was made, but none could consistently be found. The failure to find any branches of higher frequency does not preclude their existence, since other experimental difficulties (e.g., higher effective masses or poor crystal quality) may have reduced their amplitudes below a detectable level.

4.2 Some Effective Mass Results

As indicated in Equation (4.), the temperature dependence of the dHvA amplitude is expressed by the factor $X_r/\sinh X_r$, where

$$X_r = 2\pi^2 r \, m^* k_B T / e\hbar H = 147 \times 10^3 \frac{m^*}{m_0} rTH^{-1} \quad ,$$

and H is in gauss. For a constant field H, a study of the amplitude variation with temperature gives a measure of the cyclotron effective mass m^*. Although this method is not usually as precise as direct cyclotron resonance, it does have the advantage that a specific effective mass can be directly assigned to each set of oscillations.

If $X_r \gtrsim 2.2$, $\sinh X_r$ can be approximated by $e^{X_r}/2$ to within 1%, thereby allowing m^* to be determined from the slope of a graph of $\ln A/T$ versus T at constant H. Such plots are shown in Figures 16, 17, and 18, which illustrate effective masses for various frequencies at [110] and [100]. Throughout this work, the higher frequencies, although isolated from the dominant lower frequencies by analog filtering techniques, were still difficult to study because of their low amplitude; in fact, they could not be observed at $4.2°K$. The amplitude dependence with temperature of frequencies F_1 and F_8 are shown in Figure 16; the field was approximately 58 kG in both cases. The effective masses for both sets of oscillations

FIGURE 16: The amplitude dependence of the frequency terms F_1 (9.58 MG) and F_8 (20 MG) at [110]. The cyclotron effective masses have been determined to be 0.58 m_o for both terms.
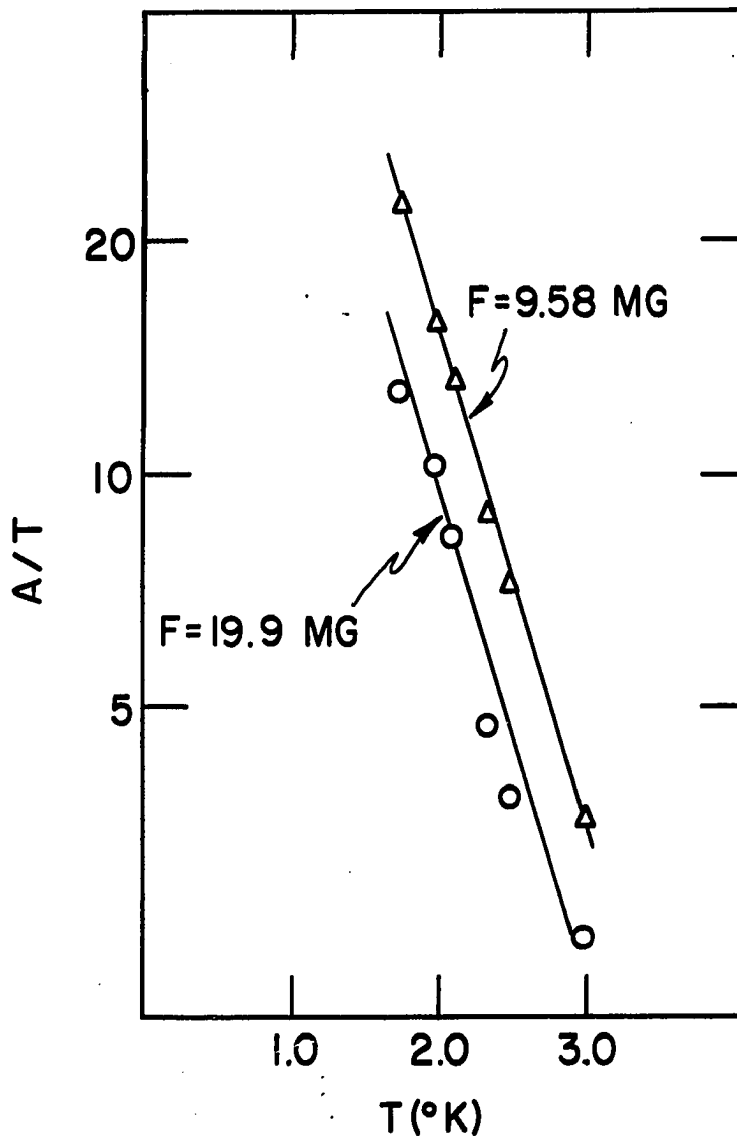
FIGURE 17: The amplitude dependence of the frequency terms F_3 and F_4, for the field direction along [100]. The slope of the semilog plot yielded effective masses of 0.66 m_o and 0.58 m_o, respectively. The amplitudes at each temperature were determined indirectly from analysis of the field-sweep beat structure (F_3 and F_4 differ by 19%) at a field of 56.7 kG.
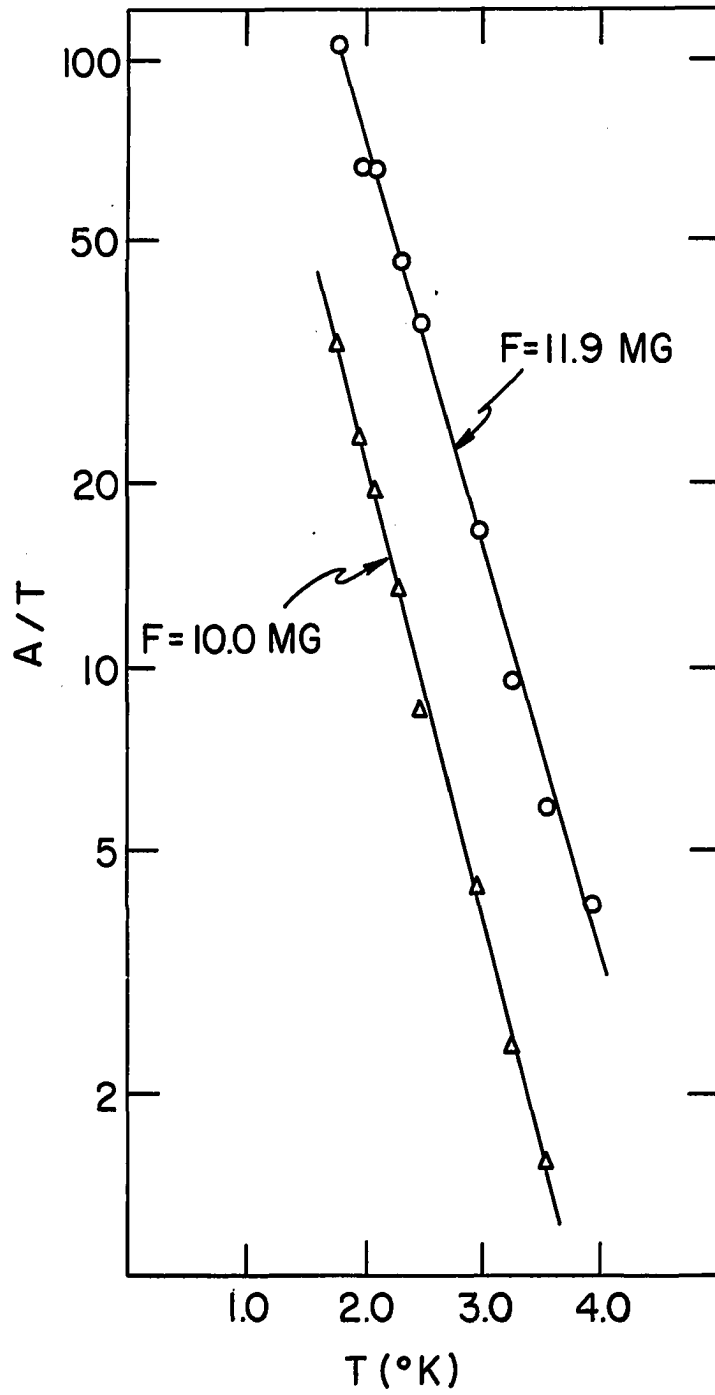
FIGURE 18: A plot of the amplitude dependence of branch F_{10} with temperature, for a 57-kG field along [100]. The effective mass was determined to be 0.75 m_o.
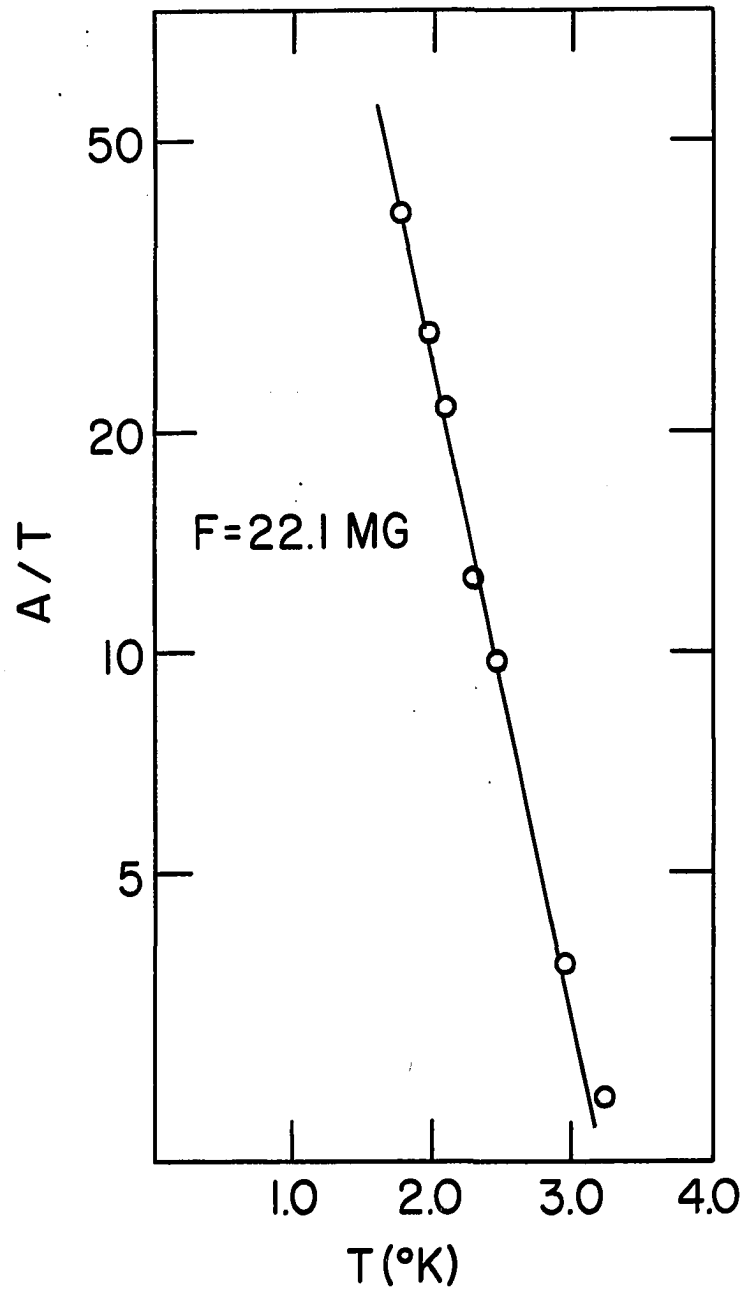
were found to have nearly equal values of 0.58 m_o.

The temperature-dependence of the amplitudes of two intermediate frequency branches F_3 and F_4 at [100] are graphed in Figure 17. The effective mass values of 0.66 m_o for the F_3 branch and 0.58 m_o for the F_4 term are subject to more error than the mass values determined for F_1 and F_8, since it was impossible to separate the two terms reliably. Because of the beat structure of F_3 and F_4, their amplitudes were studied indirectly by plotting amplitudes of beat maxima and minima, and considering maxima to be the sums of the individual amplitudes and minima to be the differences. Finally, the amplitude variation with temperature of the higher-frequency component F_{10} at [100] is plotted in Figure 18, the slope of which yields an effective mass m^* of 0.75 m_o (H = 57 kG). All of the results are summarized in Table 2.

Table 2. Determination of effective cyclotron masses at symmetry orientations

Frequency term	Orientation	m^*/m_o
F_1: 9.6 MG	[110]	0.58 ± 0.01
F_8: 19.9 MG		0.58 ± 0.03
F_3: 10.0 MG	[100]	0.66 ± 0.03
F_4: 11.9 MG		0.58 ± 0.03
F_{10}: 22.1 MG		0.75 ± 0.03

V. COMPARISON WITH THE THEORETICAL MODEL

5.1 The Electron Surface

In this chapter we compare the results discussed in Chapter IV with the model Fermi surface derived from the band calculations of Gupta and Loucks (1968). The bands calculated by these authors are sketched in Figure 19 for energies near the Fermi level. It can be seen from the figure that the intersections of the Fermi level ϵ_F with the lowest 6d band occur near Γ and L, and give rise to two hole surfaces located at these points when the entire Brillouin zone is considered (the notation for the Brillouin zone for the face-centered-cubic structure of thorium is presented in Figure 20). The Fermi level also intersects another 6d band along ΓK and ΓW, giving rise to a corresponding electron surface. It should be noted that, since the bands are relatively flat, slight changes in the bands could appreciably alter the shape of the relevant surfaces. The intersections of the above electron and hole surfaces with the Brillouin zone faces have been calculated by Gupta and Loucks, and are sketched in Figure 21.

Attention will first be given to the set of 12 butterfly-shaped electron surfaces along the ΓK directions of the Brillouin zone. A contour map in the(001) plane of one of these surfaces is drawn in detail in Figure 22, with the expected extremal cross-sections drawn as heavy lines for the symmetry directions. In Figure 22 (a.), the extremal cross-sectional areas perpendicular to the <110> directions, denoted by α, β, γ, and δ, are shown; the extremal orbits for the <100> directions are drawn in Figure 22 (b.) and are indicated by ρ, σ, and τ; and finally,

FIGURE 19: A sketch of the electron energy bands derived by Gupta and Loucks (1968). Two 6d bands intersect the Fermi level of 0.595 Ry, and a 7s band lies below.

FIGURE 20: The Brillouin zone for the face-centered-cubic crystal
lattice.
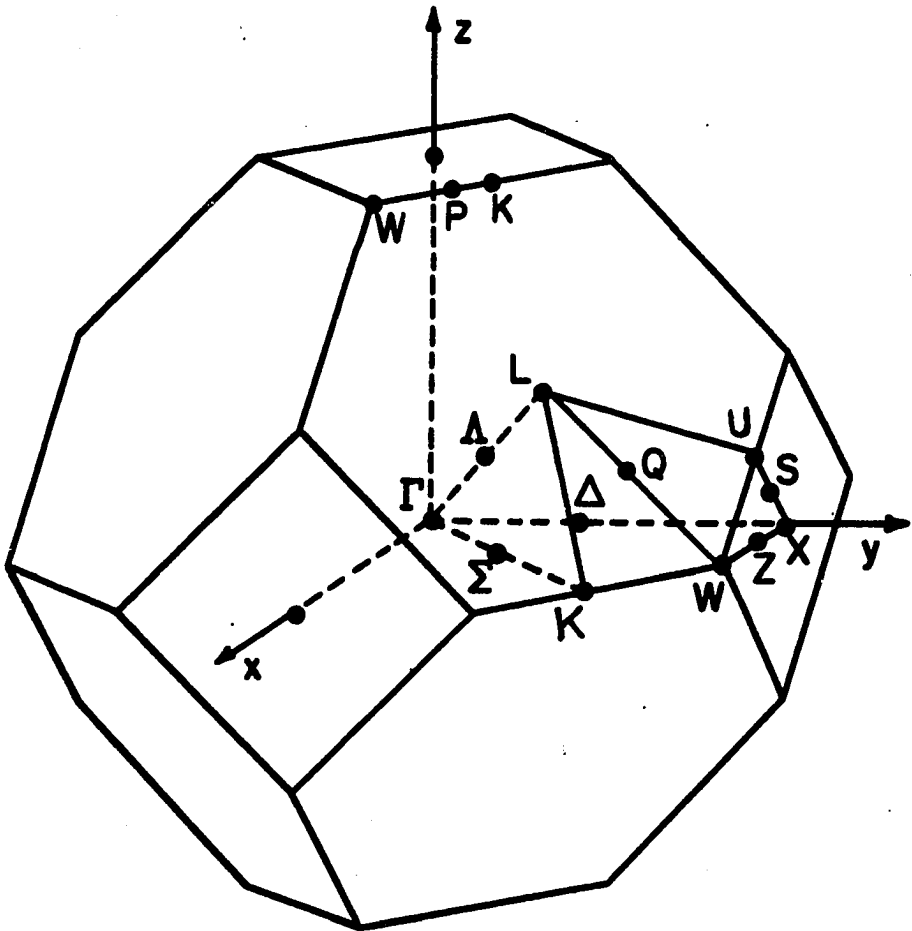
FIGURE 21: The areas of intersection of the model Fermi surface
with the faces of the 1/48 Brillouin zone outlined in
the previous figure. The electron surface is shaded.
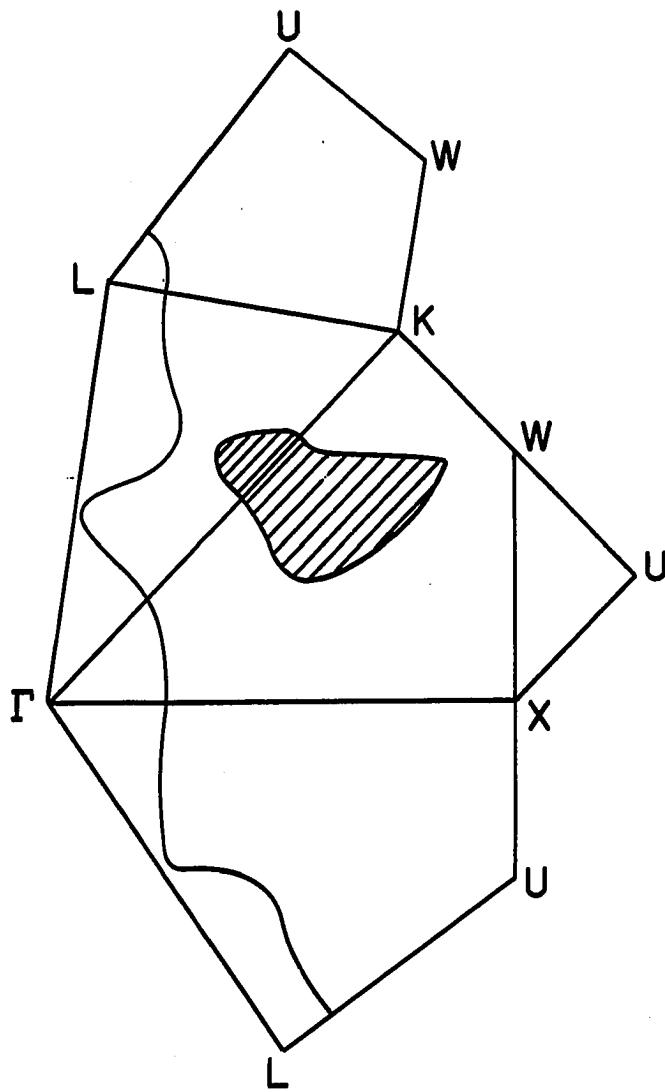
FIGURE 22: Contour maps of the electron surface of the proposed
model. The contours signify the intersections of the
Fermi surface with the planes $k_z = 0.0$ (solid line);

$k_z = 0.5$ (dashed line); $k_z = 0.8$ (solid line);

$k_z = 1.0$ (dashed lines); and $k_z = 1.2$ (solid lines),

where the unit of k is $2\pi/8a = 0.154$ ($\overset{\circ}{A}$). The
extremal cross-sectional areas perpendicular to the
symmetry directions have been found graphically and
are drawn as the heavy lines.

(a.) The extremal cross-sections for the <110>
directions are labelled as α, β, γ, and δ.

(b.) The extremal cross-sections for the <100>
directions are labelled as ρ, σ, and τ.

(c.) The extremal cross-sections for the <111>
directions are labelled as λ, μ, and ν.
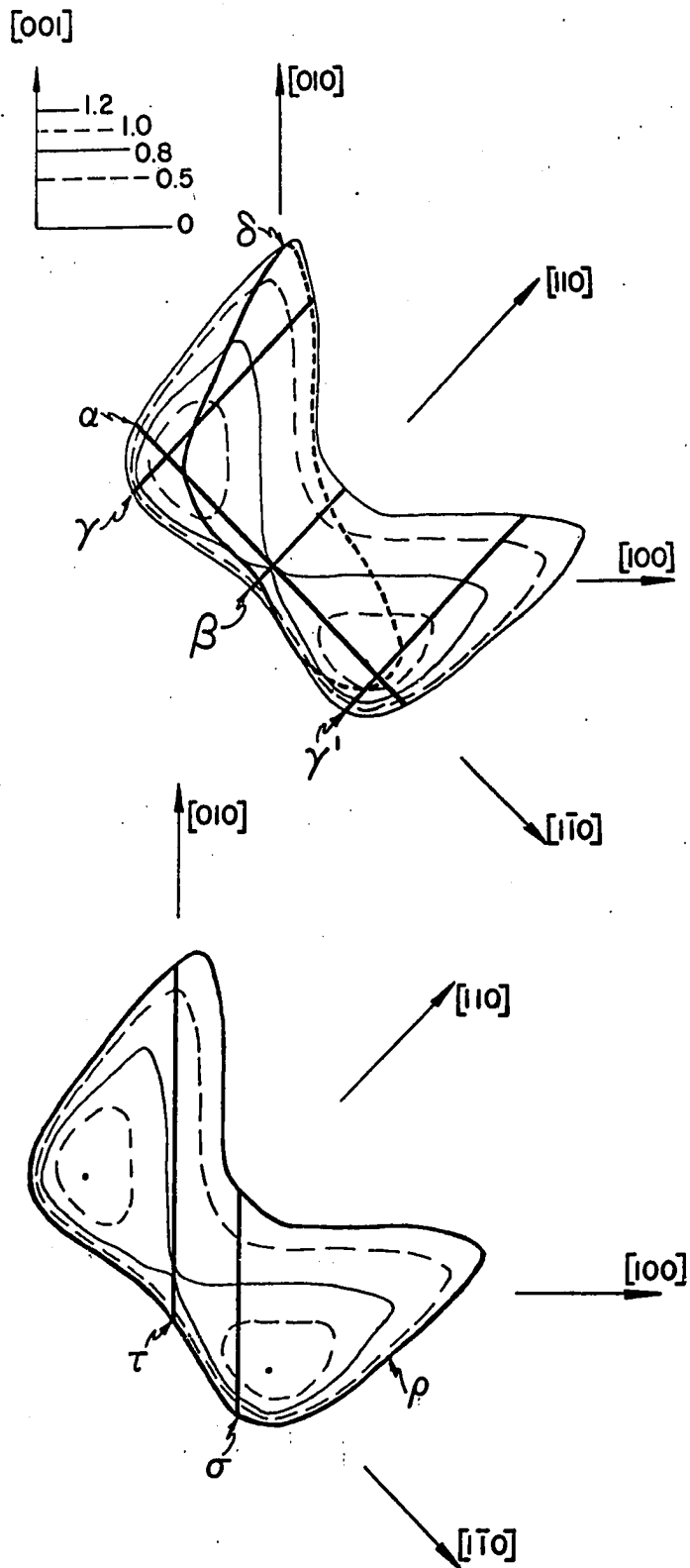
FIGURE 22:   (continued)
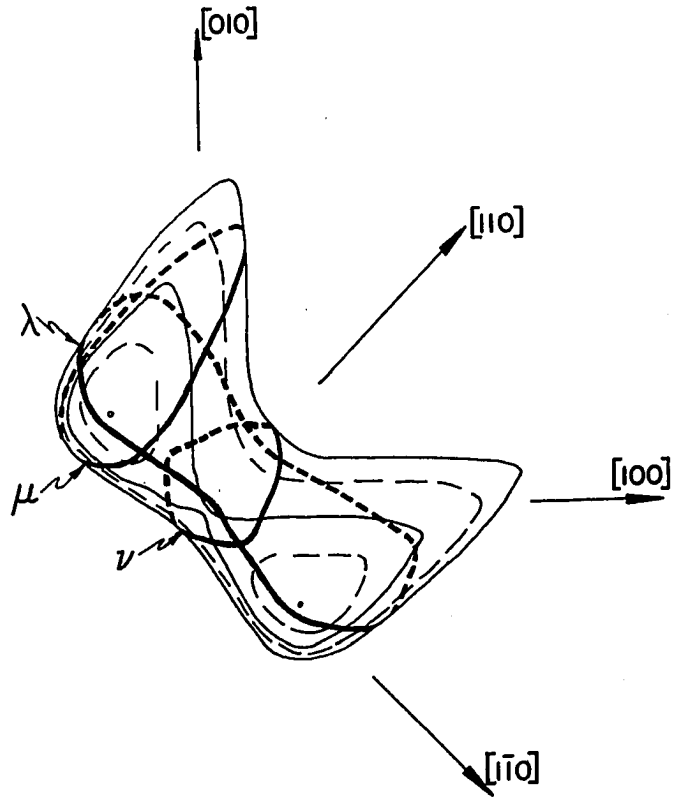
the expected extrema for the <111> directions, denoted by λ, μ, and ν, are shown in Figure 22 (c.). Since results of numerical calculations for this model Fermi surface are not yet available (these calculations are presently being made by Gupta and Loucks), the values of the above areas have been found by the more laborious graphical method. The predicted dHvA frequencies, determined with the aid of the Onsager relation (Equation (1.)), are listed in Table 3, along with the experimental frequencies measured in this work. It is clear from this table that the agreement is rather poor and that further revisions in the model are needed before a detailed analysis is possible. We will, however, present a qualitative discussion of the expected behavior of the various frequency branches of the model between symmetry directions in the (100) and (110) planes, and compare this with the experimental results.

The electron surfaces along the 12 ΓK directions present several different extremal areas for any given field direction; and rather than consider all 12 surfaces with rotation about a single symmetry axis, we will instead study a single surface and the behavior of its extremal cross-sections with rotation about all axes in a set. That is, the behavior of all 12 surfaces for rotation in the (100)-plane will be equivalent to the behavior of the single surface as rotated in the (001) and (010) planes. Similarly, the total behavior for rotation in the (110)plane will be deduced by study of the surface with rotation in the (110), ($1\bar{1}0$), and (011) planes.

With the aid of Figure 22 we consider first rotations of the field in the various {100} planes, starting with the <100> extremal orbits

Table 3. Experimental <u>vs.</u> Predicted dHvA Frequencies F for fields along the symmetry directions

SURFACE	DIRECTION	EXTREMAL TYPE	PREDICTED F	OBSERVED F
electron	<100>	inflection	σ : 8.6 MG	F_3 : 10.0 MG $\pm$ 0.05 MG
		maximum	τ : 12.5 MG	F_4 : 11.9 MG $\pm$ 0.05 MG
		maximum	ρ : 24.9 MG	
	<110>	minimum	β : 4.3 MG	F_{11}: 2.0 MG $\pm$ 0.02 MG
		maximum	γ : 11.8 MG	F_1 : 9.6 MG $\pm$ 0.03 MG
		maximum	δ : 17.8 MG	
		maximum	α : 20.0 MG	
	<111>	minimum	ν : 5.6 MG	
		maximum	μ : 11.0 MG	11.7 MG $\pm$ 0.1 MG
		maximum	λ : 20.6 MG	
hole	<100>	minimum	16.9 MG	
		maximum	20.9 MG	F_{10}: 22.1 MG $\pm$ 0.1 MG
		maximum	36.7 MG	F_{10}: 22.1 MG $\pm$ 0.1 MG
	<111>	minimum	7.9 MG	F_2' : 10.9 MG $\pm$ 0.05 MG
		maximum	12.5 MG	F_8 : 22.5 MG $\pm$ 0.5 MG
		maximum	45 MG	F_9 : 24.8 MG $\pm$ 0.1 MG
	<110>	maximum	13 MG	F_8 : 19.9 MG $\pm$ 0.1 MG
		maximum		F_9 : 24.8 MG $\pm$ 0.1 MG

σ and τ. As the field direction moves in the (001) plane, starting at [100] and ending at [1$\bar{1}$0], it can be seen that the orbit σ splits into one with a maximum area approaching γ' and one with a minimum area approaching β. In like manner, the area of orbit τ increases somewhat until it traverses the peak, and then decreases to the area of orbit γ. Whereas the orbit β has a turning value at [1$\bar{1}$0] (i.e., as rotation continues, its area increases), the two orbits γ and γ' form a crossing point at [1$\bar{1}$0]; that is, the area of γ' continues to increase with rotation, while that of γ continues to decrease. The above-mentioned behavior ($\sigma \rightarrow \beta$, γ'; $\tau \rightarrow \gamma$) is plotted in Figure 23 (a.), along with the relevant experimental data taken from the overall frequency spectrum presented in Figure 10. Thus we assign frequency F_1 to γ, F_{11} to β, F_3 to σ, and F_4 to τ. As can be seen in Figure 23 (a.), the predicted maximum in the branch $\tau \rightarrow \gamma$, caused by topological features of the model, is not reflected in the experimental data.

As further corroboration for the above assignment, consider next rotation in the opposite sense, from [100] to [110]. The orbit τ now begins to increase continuously in area and eventually reaches the area of orbit α, which has a turning value at [110]. Orbit σ was formed by an inflection point of cross-sectional area at [100], and is soon lost with this rotation. The resulting behavior is compared with the experimental data in Figure 23 (b.). Finally, consider rotation about the [010] axis. The orbits τ and σ appear to increase in area until the single maximum cross-sectional area of δ is reached at [101]; as rotation continues, the orbit continues to increase in area to that of

FIGURE 23: Comparison of frequencies between the model and the experiment, for rotations of the electron surface in the $\{100\}$ plane.

(a.) A sketch of the predicted variations in frequency arising from the model as the field is rotated clockwise in the (001) plane, along with a plot of the corresponding experimental data as presented in Figure 10. The frequency bands F_{11}, F'_3, and F_5 have been assigned to the variations $\sigma \to \beta$, $\sigma \to \gamma$, and $\tau \to \gamma$.

(b.) Frequency comparisons for counterclockwise rotation in the (001) plane. The frequency branch F_{13} has been identified with the variation $\tau \to \alpha$.

(c.) Corresponding frequencies for rotation of the field in the (010) plane. The frequency terms F_6 and F_{14} have been assigned to the variations $\sigma \to \delta$ and $\tau \to \delta$.

ANGLE FROM [110] (DEGREES)

a.   b.   c.
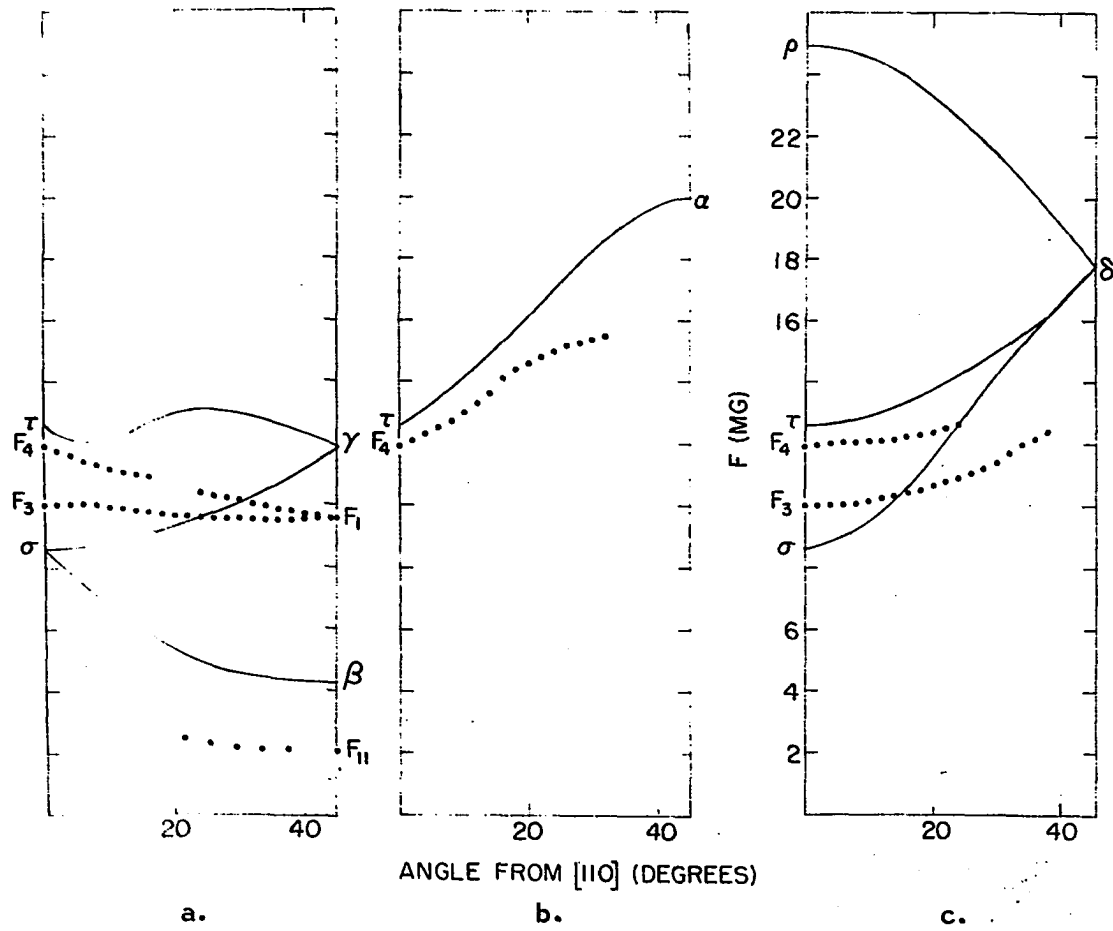
ρ when the field is along [001]. These expected variations are plotted

in Figure 23 (c.), together with the pertinent experimental data. Al-

though the magnitudes of the theoretically determined and experimentally

derived frequencies do not agree, the qualitative behavior predicted

from the model is in good general agreement with that of the observed

frequency branches. Unfortunately, the qualitative agreement is not

complete, since no experimental evidence for the existence of the

orbits α, δ, and ρ has been found.

Turning now to the {110}-plane rotations, we consider first a

rotation about the [110] axis, beginning with the two extremal orbits

β and γ for the field direction along [1$\bar{1}$0] (see Figure 22 (a.)); as

the [001] field direction is reached, these orbits coalesce into a

single orbit ρ. We idertify the frequency branch F_1 with the orbit

variation γ→ρ, as shown in Figure 24 (a.); although the predicted

variation of γ near [110] does not agree with the variation of F_1

(i.e., $F_1 \propto 1/\cos \theta$), it is possible that the actual surface is fluted

in the vicinity of the relevant orbits in order to permit the observed

behavior of F_1. Again, we identify the frequency branch F_{11} with the

orbit β, although F_{11} is difficult to follow in this plane. If we now

rotate the field about the [1$\bar{1}$0] axis, starting at [110], the area of

α is expected to increase to that of ρ at [001], and this variation is

also shown in Figure 24 (a.). As before, we have been unable to find

any experimental evidence for the orbits α and ρ.

Lastly, we consider the field to be rotated in the (011) plane,

beginning with the orbits τ and σ for H along [100]. As the field is

FIGURE 24: Comparison of frequencies between the model and the experiment, for rotations of the electron surface in the {110} plane.

(a.) For rotation of the field in the (110) plane, frequency branches F_{11} and F_1 have been identified with the model variations of the extremal orbits $\beta \to \nu \to \rho$. For rotation in the ($1\bar{1}0$) plane, however, no experimental data has been found to correspond to the variation $\alpha \to \lambda \to \rho$.

(b.) As the field is rotated in the (011) plane, the frequency branches F_3, F_4, and F_2 have been assigned to the model variations $\sigma \to \mu$, $\tau \to \mu$, and $\mu \to \delta$. Several data points also suggest a correspondence to the variations $\tau \to \lambda \to \delta$ and $\sigma \to \nu \to \delta$.
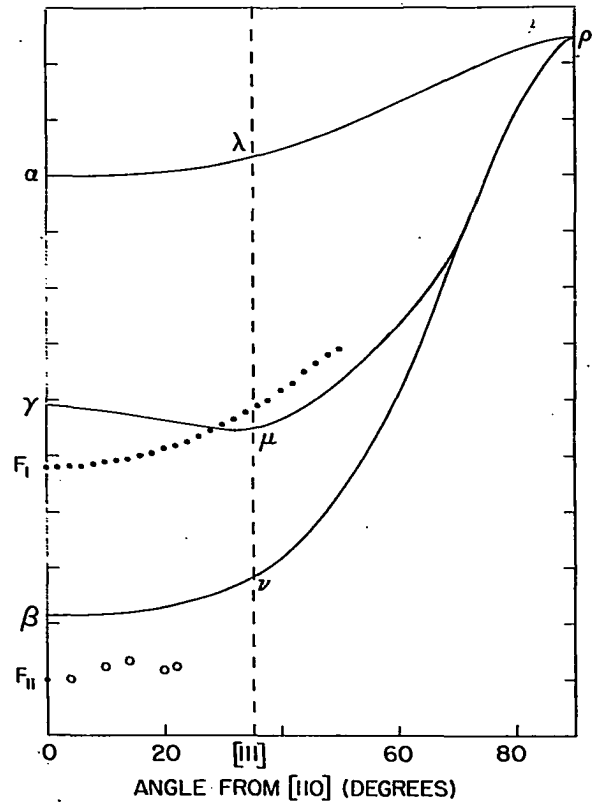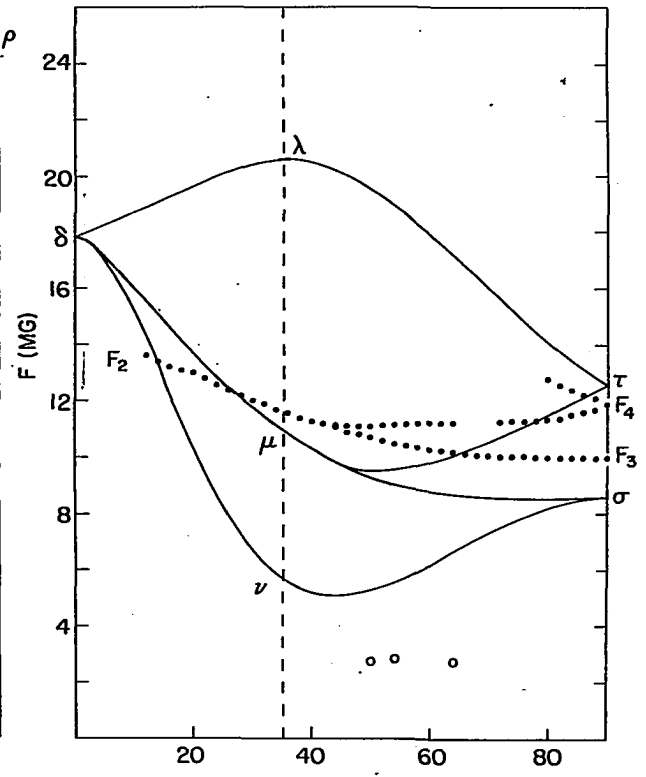
rotated toward [0̄11], the orbits τ and σ form the orbits μ and ν as

seen from [1̄11] , and finally coalesce into the orbit δ as seen from

[01̄1]. For a field rotation in the opposite sense, we have a continua-

tion through orbit λ as seen from [11̄1̄], and back to the orbit δ as

viewed from [01̄1̄]. These results are plotted in Figure 24 (b.), where

we assign the frequency branch F_2 to the variation δ → μ, F_4 to μ → τ,

and F_3 to μ → σ. Thus we expect that, regardless of the topological

details, the symmetry of the model requires that the relevant frequencies

cross at <111> with a common value μ; such a crossing for the branches

F_1 and F_2 is in fact observed experimentally, as can be seen in the

composite frequency spectrum in Figure 10.

5.2 The Hole Surface

As mentioned above, we have found no experimental evidence for the

orbits α, ρ, and δ predicted by the electron surface of the Gupta-Loucks

model, except for the possibility of explaining the dHvA frequencies

observed in the 20-25 MG range by ascribing F_{10} to ρ, F_8 to δ, and

F_9 to α. However, the electron-surface model predicts no connection

between α and ρ in the (100) plane, while the branches F_8 and F_9 actually

merge to F_{10} at [100]; there appears to be no simple alteration in the

model which would result in such a connection. Furthermore, the assign-

ments of the model for the previously-considered lower frequencies seem

to imply that the α- and δ- orbits should in reality be decreased in area.

Therefore, we will consider the dHvA frequency branches arising from the

hole surface of the model, and study the high-frequency experimental data

in terms of this surface.

As shown in Figure 21, a small neck connects the rounded cube centered at Γ with the dumbbell-shaped surface located at L; more detailed band calculations, as well as the absence of experimentally observed low-frequency oscillations which could be attributed to this neck, leads us to suppose that the connection is absent, and that the two pieces of hole surface are separate.

A portion of the hole surface consists of dumbbell-shaped arms centered at the point L of the Brillouin zone with axes along [111]. The minimum central cross-sectional area produces a dHvA frequency of 7.9 MG when the field direction is along [111], and the maximum non-control cross-sectional areas correspond to a dHvA frequency of 12.5 MG. As noted earlier (page 59), the frequency branch F'_2 varies as the central minimum cross-sectional area of such a dumbbell, having an observed frequency of 10.9 MG for $\underline{H}$ along [111]. If we now assign F'_2 to the corresponding orbit of the model, we infer that its area is to be increased by a factor of $10.9/7.9 \approx 1.4$, and thus we expect that the corresponding non-central area might also be increased by roughly this factor. The only branch of higher frequency observed that has the required symmetry expected for the quasi-spherical ends of a dumbbell oriented along [111] is F_8, which exhibits this symmetry throughout the (110) plane. This branch has a value of 22.5 MG at [111], and this would correspond to a scaling factor of 1.8 over the model. The expected frequency variations in the (110) and (100) planes of such a dumbbell surface (appropriately scaled up from the Gupta-Loucks model) are plotted schematically in Figure 25 as the solid lines. The dHvA frequency

FIGURE 25: The comparison of frequency branches F_2', F_8, and F_9 to the hole surface of the Gupta-Loucks model. The solid lines denotes frequency variations arising from the dumbbell-shaped portions located at the points L of the Brillouin zone; this surface has been scaled up in size to fit the frequency values of F_2' and F_8 at [111]. The sheet centered at Γ is thought to be scaled down and revised in shape to fit the frequency branch F_9.
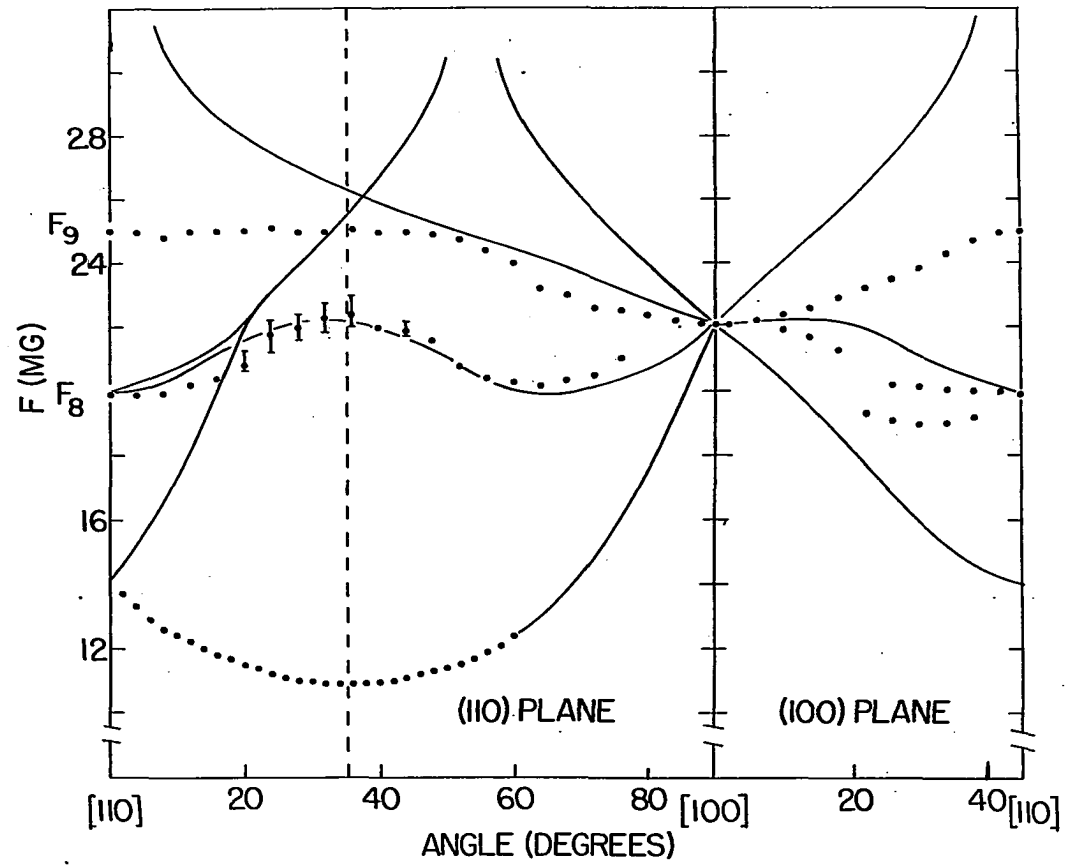
corresponding to the cross-sectional area of the profile of this proposed

dumbbell (i.e., with $\underline{H}$ in a direction perpendicular to the axis along

[111]) would be higher than any of those detected. As with the previous

discussion of the electron surface, we are handicapped by the fact

that the branch F_2' cannot be followed to its projected coalescence with

the higher-frequency branches.

We follow Thorsen et al. (1967) in proposing that the remaining

frequency branch F_9 is due to an orbit around the hole surface centered

at Γ. Such an assignment requires that this sheet of the Fermi surface

would be scaled down from the dimensions of the Gupta-Loucks model

(see Table 3). This scaling is plausible, since in order to preserve

compensation the previously-asserted increase in the volume of the dumb-

bell-shaped arms would imply a decrease in the volume of the central

section at Γ. If we further modify the original cubical shape of the

Gupta-Loucks model to a quasi-spherical shape, with flattened regions on

the (100) faces and raised bumps in the [111] directions (the latter

being reminiscent of the connectivity along ΓL of the original model),

then such a surface could have the same cross-sectional area at [111]

as at [110], and a reduced area at [100], as suggested by the experimental

data.

In conclusion, it is felt that the experimental observations are

in good agreement with the Gupta-Loucks model of the electron surface.

In regard to topological details, it appears that the areas of the model

orbits β, γ, and τ should be reduced, whereas those of orbits σ and μ

should be increased. This can be done by increasing the dimensions of

the model in the [001] direction, and decreasing those in the [110]
direction. Some of these dimensional difficulties might be resolved if
the intermediate-range frequency branches could be experimentally
pursued to the symmetry values corresponding to the predicted extremal
areas of α and δ for $\underline{H}$ along [110], and to that of ρ for $\underline{H}$ along [100].
Agreement is less satisfying in the case of the hole surface, and it
appears that the dumbbell-shaped arms along ΓL are significantly larger
than predicted, that the central surface is smaller, and that the two
surfaces are disconnected. Again, these problems may be resolved if
the frequency branch F_2' could be followed throughout the (110) plane.
The need to preserve compensation also arises, especially if the 6d
bands are shifted to generate the suggested revisions of the Fermi
surface.

As mentioned in the previous chapter, the values of m^*/m_o correspond-
ing to the observed dHvA oscillations were found to be less than unity,
and it is possible that the effective masses for the undetected frequen-
cies would exceed those corresponding to the observed frequencies. The
amplitude reduction resulting from such an increase in m^* could account
for the failure to follow many of the frequency branches throughout the
planes.

VI. CONCLUSIONS AND SUGGESTIONS FOR FUTURE STUDY

In this investigation, the de Haas-van Alphen effect in thorium has been extensively studied, using the modulated-field technique and monitoring the main field with the n.m.r. All field sweeps were recorded digitally, and subsequent analysis by the periodogram technique enabled the detection of many frequency terms which normally would have been below the noise level. Direct study of rotation curves at constant fields not only facilitated the tracking of the individual frequency branches, but also established the crossing and turning points of these branches at the symmetry directions; such topological features must be contained in the behavior of any theoretical model proposed for the Fermi surface of thorium. The various frequency branches qualitatively deduced from the Gupta-Loucks model have been compared with the observed frequency branches, and the behavior of the electron surface of the model has been found to be in good general agreement with the lower (i.e., less than 14 MG) dHvA frequencies. However, major revisions of the proposed hole surfaces are necessary to adequately account for the higher dHvA frequencies.

All of the measured cyclotron effective masses were found to be less than the free electron mass, and many of the corresponding terms were difficult to detect in the present investigation. Thus, other dHvA frequency terms with higher effective mass may exist, and a vigorous attempt should be made to find such oscillations, using crystals of higher purity and perfection, as well as further exploitation of the frequency discrimination techniques mentioned in Chapter II.

The connectivity of the two hole surfaces along L suggested by the Gupta-Loucks model would appear not to exist, according to the present dHvA data. Measurements of the magnetoresistance of thorium single crystals would clarify this point (i.e., such a connectivity would give rise to open orbits in the $\langle 111 \rangle$ direction). Lastly, a recomputation of the energy bands using experimentally derived parameters would be desirable and should help in an understanding of the actual form of the Fermi surface of thorium.

VII. LITERATURE CITED

Berlincourt, T. G.
1959 Hall effect, resistivity, and magnetoresistivity of Th, U, Zr, Ti, and Nb. Phys. Rev. 114: 969.

Chambers, R. G.
1966 The wave function of a Bloch electron in a magnetic field. Proc. Phys. Soc. (London) 89: 695.

Clusius, K and Franzosini, P.
1956 Zur Atom- und Electronenwärme des Th. Zeitschrift für Naturforschung. 11a: 957.

Cooley, J. W. and Tukey, J. W.
1965 An algorithm for the machine calculation of complex Fourier series. Math. Comp. 19: 297.

Decker, W. R., Peterson, D. T., and Finnemore, D. K.
1967 Meissner effect for superconductors with magnetic impurities. Phys. Rev. Letters 18: 899.

Dooley, G. J.
1966 Electrical resistivity of pure thorium and some thorium-carbon alloys. Unpublished M. S. thesis. Ames, Iowa, Library, Iowa State University of Science and Technology.

Fletcher, G. C. and Wohlfarth, E. P.
1951 Calculation of the density of states curve for the 3d electrons in nickel. Phil. Mag. 42: 106.

Girvan, R. F., Gold, A. V., and Phillips, R. A.
1968 The de Haas-van Alphen effect and the Fermi surface of tungsten. [To be published in J. Phys. Chem. Solids ca. 1968.]

Gold, A. V.
1968 The de Haas-van Alphen effect. [To be published in the 1967 Simon Fraser Summer Institute Proceedings ca. 1968.]

Gordon, J. E., Montgomery, H., Noer, R. J., Pickett, G. R., and Tobón, R.
1966 Superconductivity of thorium and uranium. Phys. Rev., 152: 432.

Gupta, R. P. and Loucks, T. L.
1968 Relativistic energy bands and the Fermi surface of thorium. [To be published in Phys. Rev. Letters ca. 1968.]

Hill, D. A. and Hwang, C.
1966 Measurement of magnetic fields at liquid helium temperatures. Jour. Sci. Instrum. 43: 581.

Hodges, L., Stone, D. R., and Gold, A. V.
   1967 Field-induced changes in the band structure and Fermi surface
         of nickel. Phys. Rev. Letters 19: 655.

Keeton, S. C.
   1966 Relativistic energy bands and Fermi surface for some heavy
         elements. Unpublished Ph.D. thesis. Ames, Iowa. Library,
         Iowa State University of Science and Technology.

Keeton, S. C. and Loucks, T. L.
   1966 Relativistic energy bands for thorium, actinium, and lutetium.
         Phys. Rev. 146: 429.

Lehman, G. W.
   1959 Effect of spin-orbit coupling on energy levels in the 6d band
         for actinide metals. Phys. Rev. 116: 946.

Lifshitz, T. M. and Kosevich, A. M.
   1956 Theory of magnetic susceptibility in metals at low temperatures.
         Soviet Physics JETP 2: 636.

Onsager, L.
   1952 Interpretation of the de Haas-van Alphen effect. Phil. Mag.
         43: 1006.

Panousis, P. T.
   1967 The de-Haas-van Alphen effect and the Fermi surface of iron.
         Unpublished Ph.D. thesis. Ames, Iowa, Library, Iowa State
         University of Science and Technology.

Pippard, A. B.
   1965 Dynamics of conduction electrons. New York, Gordon and Breach.

Peterson, D. T., Schmidt, F. A., and Verhoeven, J. D.
   1966 Electrotransport of carbon, nitrogen, and oxygen in thorium.
         Transactions of Metallurgical Society of AIME 236: 1311.

Shoenberg, D. and Stiles, P. J.
   1964 The de Haas-van Alphen effect in alkali metals. Proc. Roy.
         Soc. (London) A281: 62.

Stark, R. W.
   1967 Fermi surface of magnesium. II. The de Haas-van Alphen effect.
         Phys. Rev. 162: 589.

Stone, D. R.
   1967 Field modulation studies of the de Haas-van Alphen effect in
         nickel. Unpublished Ph.D. thesis. Ames, Iowa, Library, Iowa
         State University of Science and Technology.

Thorsen, A. C., Joseph, A. A., Valby, L. E.
    1967 de Haas-van Alphen effect and Fermi surface in thorium. Phys.
        Rev. 162: 574.

Windmiller, L. R. and Priestley, M. C.
    1965 The Fermi surface of antimony. Solid State Comm. 3: 199.

Finally, I wish to thank my parents, Mr. and Mrs. Orland Boyle, for their constant interest and encouragement.

IX.   APPENDIX I.

FIGURE 26: An annotated version of the Panousis program for the analysis of dHvA
frequencies by the filter-periodogram method. This program has been
modified for use with data collected by the modulated-field technique.

```
C     THIS PROGRAM ANALYSES LINEARLY-RAMPED MODULATED-FIELD DE HAAS-
C     VAN ALPHEN DATA BY MEANS OF FREQUENCY FILTER RESPONSE SYNTHESIS,
C     FOLLOWED BY PERIODOGRAM ANALYSIS.  THE FREQUENCIES AND RELATIVE
C     AVERAGE INTENSITIES ARE PRINTED OUT AND PLOTTED.
C
C     BOYLE      ACCOUNT A0026     CRYSTAL PHYSICS VII, AMES LAB.     ISU
C
C     THIS IS THE MAIN PROGRAM.
C
C     THE DIMENSION STATEMENTS BELOW ALLOW FOR 200 FILTER PASSFREQUENCIES
C     (UU), 200 FILTER INTENSITIES (ZZ), AND 200 PERIODOGRAM INTENSITIES
C     (Z).    SPACE IS ALSO ALLOTED FOR 100 FILTER RESPONSE MAXIMA (UU2, Z2)
C     AND 100 PERIODOGRAM RESPONSE MAXIMA (UU1,Z1).
C
      DOUBLE PRECISION DRH
      DIMENSION UU1(100),Z1(100),UU2(100),Z2(100),Z(200),ZZ(200)
      DIMENSION UU(200)
      DIMENSION HEAD(10)
      DIMENSION ARRAYT(7)
      DIMENSION XLAB1(5),YLAB1(5),GLAB1(5),GLAB2(5)
      COMMON XLAB(5),YLAB(5),Y(10005)
      KS=1547714624
      IMIN=1
      LMAX=0
      OUTRA=10.**30
C     THE FIRST CARD IN THE DATA GIVES AXIS LABELS FOR GRAPHING THE
C     INPUT DATA.  THIS IS THE ONLY TIME THIS SET OF LABELS IS READ IN,
C     EVEN FOR MORE THAN ONE DATA SET.
      READ (1,6) XLAB,YLAB,XLAB1,YLAB1
    6 FORMAT (20A4)
    1 FORMAT (2F5.0,3F6.0,2F4.0,2I2,10A4)
    2 FORMAT ('1    DE HAAS-VAN ALPHEN COMPUTATIONS--    DATA SET NUMBER
     1',12A4)
    3 FORMAT ('0    RATE=',F4.0,' KCPS.    HSCALE=',F6.4,'     HZERO=',F6.0
     1,' GAUSS    THETA=',F7.2,' DEG.     COILK=',F6.0,' GAUSS/VOLT    TZE
```

FIGURE 26: (continued)

```
      1RO=',F4.0,' MSEC.')
C     ON THE SECOND CARD, CONTROL NUMBERS AND LABELS FOR THE DATA SET ARE READ.
C     RATE=-1 FOR THIS PROGRAM.  HSCALE,TZERO,NADD USUALLY ARE NOT USED.
C     HZERO SPECIFIES THE FERROMAGNETIC INTERNAL FIELD (OR SOLENOID OFFSET),
C     THETA SPECIFIES THE FIELD ROTATION ANGLE FOR FERROMAGNETS.
C     QQQ IS THE FILTER Q (SET BY PROGRAM TO 10 IF NOT SPECIFIED).
C     HEAD IS THE DATA SET LABEL (40 SPACES ALLOTED).
C
    4 READ (1,1) RATE,HSCALE,HZERO,THETA,COILK,TZERO,QQQ,MPTS,NADD,
    1(HEAD(I),I=1,10)
    5 WRITE (3,2) (HEAD(I),I=1,10)
    9 DO 8 I=1,5
      GLAB1(I)=HEAD(I)
    8 GLAB2(I)=HEAD(I+5)
      DELT=0.0
      CALL STARTM(DELT)
      HSCALE=HSCALE/10000.
      THETA=THETA/100.
      WRITE (3,3) RATE,HSCALE,HZERO,THETA,COILK,TZERO
      PIE=3.14159
      TZERO=TZERO/(10.**6)
      THETA=THETA*PIE/180.
      NDEG=3
      IF (QQQ) 731,731,732
  731 QQQ=10.
  732 CONTINUE
      CALL DATE(ARRAYT)
      WRITE (3,103) ARRAYT
  103 FORMAT (4X,7A4)
      IF (RATE) 300,200,100
  100 DT=1./(RATE*1000.)
      GO TO 400
  200 CONTINUE
      GO TO 400
  300 CALL STEADF (QQQ,MPTS,DRH,H1,THETA,HZERO,HEAD,FFIRST,FLAST,RES,
```

FIGURE 26: (continued)

```
      1TI MEN,KMAX,NPTS)
  400 CONTINUE
      RES1=RES*100.
  601 FORMAT ('0         LOWEST FREQUENCY CONSIDERED WAS  =',E10.3)
  602 FORMAT ('          HIGHEST FREQUENCY CONSIDERED WAS =',E10.3)
  603 FORMAT ('          RESOLUTION                       =',F6.3,'
     1PERCENT')
  606 FORMAT ('          THE FILTER Q                     =',F3.0)
  607 FORMAT ('          THE NUMBER OF SUBDIVISIONS IS    =',I3)
C
C     THE CONTROL NUMBERS 'NFIRST' AND 'NLAST' ARE SET UP.  NFIRST IS THE NUMBER
C     OF POINTS PER CYCLE OF FFIRST THAT THE DATA CONTAIN.  NCOL IS EQUAL TO
C     THE NUMBER OF POINTS PER CYCLE OF THE FILTER PASSFREQUENCY.
C     THE BASIS FOR THE PERIODOGRAM IS BEING SET UP HERE.     FFIRST AND FLAST
C     ARE REDEFINED SO THAT EXACTLY NFIRST AND NLAST POINTS PER CYCLE OF EACH
C     EXIST.       NSTEP IS ROUGHLY PROPORTIONAL TO RES AND TO NLAST (TO AVOID
C     MORE THAN 200 PASSES THROUGH THE FILTER) AND HAS AN ABSOLUTE VALUE OF
C     AT LEAST 1.  MORE PASSES THROUGH THE FILTER THAN THE NUMBER SET UP HERE
C     CAN BE DONE BY REDUCING RES OR BY INCREASING NPTS AT THE START.
C
      NFIRST=1./(DRH*FFIRST)
      FFIRST=1./(DRH*NFIRST)
      NLAST=1./(DRH*FLAST)
      FLAST=1./(DRH*NLAST)
      NSTEP=1+NLAST*RES
   32 FORMAT ('0     DRH=',E10.3,'     NFIRST=',I6,' NLAST=',I6,' NSP',I3)
      WRITE (3,32) DRH,NFIRST,NLAST,NSTEP
  608 NCOL=NFIRST
      UO=2.*PIE*FFIRST
      WRITE (3,601) FFIRST
      WRITE (3,602) FLAST
  605 WRITE (3,606) QQQ
      WRITE (3,603) RES1
  609 WRITE (3,607) MPTS
      I=1
```

FIGURE 26: (continued)

```
      305 CALL FILTER (OUT,IMIN,NPTS,DRH,UO,QQQ,NCOL,KMAX,OUT2)
          IF (OUT-OUTRA) 690,690,691
      691 WRITE (3,692)
      692 FORMAT ('0********** THE SPECTRUM IS DIVERGENT **********')
          GO TO 307
      690 Z(I)=OUT
          ZZ(I)=OUT2
          UU(I)=UO/(2.*PIE)
          IF (I-200) 725,725,824
      824 WRITE (3,825)
      825 FORMAT ('0 ********** RESOLUTION TOO HIGH **********')
          GO TO 307
      725 I=I+1
C         NCOL AND UO  ARE CHANGED, AND THE FILTER IS AGAIN CALLED.
          NCOL=NCOL-NSTEP
          UO=2.*PIE/(DRH*NCOL)
       11 IF (NCOL-NLAST) 307,305,305
      307 CONTINUE
          LLL=I-1
          CALL FIT (LLL,ZZ,UU,UU2,Z2,RATIO,LK2)
      101 FORMAT (61X,'    END OF FILTER FIT.')
          WRITE (3,101)
          CALL FIT (LLL,Z,UU,UU1,Z1,RATION,LK)
C         THE FILTER SPECTRUM IS ADJUSTED TO BE PLACED IN A LOWER GRAPH.
          DO 1010 I=1,LLL
     1010 ZZ(I)=ZZ(I)-1.
          DO 427 I=1,LK2
      427 Z2(I)=Z2(I)/RATIO
          DO 418 I=1,LK
      418 Z1(I)=Z1(I)/RATION
      428 WRITE (3,415) RATION
          WRITE (3,1000) RATIO
      415 FORMAT ('            NORMALIZING FACTOR (PERIODOGRAM) =',E10.3)
     1000 FORMAT ('            NORMALIZING FACTOR (FILTER)      =',E10.3)
          IF (MPTS) 430,426,426
```

FIGURE 26: (continued)

```
C       THE PERICDOGRAM SPECTRUM IS GRAPHED.
  426 CALL GRAPH (LLL,UU,Z ,KS,3,12.,10.,0,0,0.2,-1.0,XLAB1,YLAB1,
     1GLAB1,GLAB2)
  430 WRITE (3,416)
  416 FORMAT ('0')
C       THE FILTER MAXIMA ARE PRINTED CUT.
      WRITE (3,1001)
 1001 FORMAT ('0          FILTER ANALYSIS')
      WRITE (3,417)
  417 FORMAT ('0          FREQUENCY          INTENSITY')
      WRITE (3,419)
  419 FORMAT (' ')
      DO 1005 I=1,LK2
 1005 WRITE (3,1006) UU2(I),Z2(I)
 1006 FORMAT (E20.5,E19.5)
      WRITE (3,1015)
 1015 FORMAT ('0')
C       THE PERIODOGRAM MAXIMA ARE PRINTED, USING A NOISE LEVEL OF 0.05.
 1002 FORMAT ('0          PERIODOGRAM ANALYSIS')
      WRITE (3,1002)
      WRITE (3,417)
      WRITE (3,419)
      I=1
      LLLLK=LK
  800 IF (Z1(I)-0.05) 801,802,802
  802 I=I+1
      IF (I-LLLLK) 800,800,820
  801 IF (I-LLLLK) 804,806,806
  804 LLLLK=LLLLK-1
      DO 803 K=I,LLLLK
      Z1(K)=Z1(K+1)
  803 UU1(K)=UU1(K+1)
      GO TO 800
  806 LLLLK=LLLLK-1
  820 DO 420 I=1,LLLLK
```

FIGURE 26: (continued)

```
  420 WRITE (3,421) UU1(I),Z1(I)
  421 FORMAT (E20.5,E19.5)
      IF (MPTS) 461,431,431
C     THE FILTER SPECTRUM IS GRAPHED.
  431 CALL GRAPH (LLL,UU,ZZ,KS,3,0.,10.,0,0,0.2,-1.C,0,0,0,0)
  461 CONTINUE
      CALL STOPTM(DELT)
      WRITE (3,699) DELT
  699 FORMAT (62X,'  TIME USED IN EXECUTICN  (SEC)', F8.2)
      IF (LMAX) 424,424,422
  422 WRITE (3,423)
  423 FORMAT ('1           CCNTINUATICN OF PREVIOUS DATA SET FOR FALLING FI
     1ELD')
      HSCALE = HSCALE*10C00.
      GO TO 5
  424 CONTINUE
      QQQ=0.
      F1=0.
      F2=0.
      RES=0.
      MPTS=0
C     THE FIRST CARD OF THE NEXT DATA SET IS READ.  IF THIS CARD IS A BLANK,
C     THE PROGRAM ENDS.
      READ (1,1) RATE,HSCALE,HZERO,THETA,COILK,TZERO,QQQ,MPTS,NADD,
     1(HEAD(I),I=1,10)
  501 IF (RATE) 5,450,5
  450 IF (COILK) 5,451,5
  451 WRITE (3,452)
  452 FORMAT ('1           END OF DATA    PANOUSIS   22C RES.   TELE 4-6816')
      STCP
      END
```

FIGURE 26: (continued)

```
      SUBROUTINE FIT (LLL,Z,UU,UU1,Z1,RATION,LK)
C     THIS SUBROUTINE FINDS PEAKS IN THE LLL-ELEMENT FREQUENCY-RESPONSE
C     ARRAY (Z VS. UU) AND FITS A SECOND-ORDER CURVE THROUGH THE MAX AND TWO
C     NEIGHBORING POINTS, TO FIND THE ABSOLUTE MAX (Z1) AND CORRESPONDING
C     FREQUENCY (UU1).  THE NUMBER OF MAXIMA IS KEPT (LK) AND THE HIGHEST
C     MAXIMUM VALUE (RATION) IS FOUND, FOR NORMALIZATION PURPOSES.
      DIMENSION Z(200),UU(200),Z1(99),UU1(99)
      DIMENSION X1(3),X2(3),W(3)
      DOUBLE PRECISION A(4)
      IF (Z(1)) 2,100,100
    2 DO 5 I=1,LLL
    5 Z(I)=-Z(I)
  100 Z1(2)=C.
      K=1
      I=1
      IF (Z(2)-Z(1)) 405,401,401
  401 IF (Z(I+1)-Z(I)) 403,403,402
  402 I=I+1
      IF (I-LLL) 401,410,410
  403 DO 404 J=1,3
      NM=I+J-2
      W(J)=1.0
      X1(J)=UU(NM)
  404 X2(J)=Z(NM)
      CALL CPLSPA (2,3,X1,X2,W,A,0.0)
      UU1(K)=-A(2)/(2.*A(3))
      Z1(K)=A(1)-(A(2)*A(2))/(4.*A(3))
      IF (K-99) 842,844,844
  844 WRITE (3,846)
  846 FORMAT ('0 ********** THERE ARE MORE THAN 99 PEAKS **********')
      GO TO 410
  842 K=K+1
  405 IF (Z(I+1)-Z(I)) 406,401,401
  406 I=I+1
      IF (I-LLL) 405,410,410
```

FIGURE 26:   (continued)

```
  410 LK=K-1
      IF (LK) 430,430,432
  430 WRITE (3,431)
  431 FORMAT ('0          THERE ARE NO PEAKS IN THIS DATA SET')
C         IF THE PROGRAM GOES THROUGH THE RESPONSES AND FINDS NO PEAKS  (I.E.
C         MONOTONIC) IT SETS LK=1 AND RATION=LARGEST Z.
      LK=1
      IF (Z(LLL)-Z(1)) 4,3,3
    3 Z1(1)=Z(LLL)
      GO TO 432
    4 Z1(1)=Z(1)
      RATION=Z1(1)
      GO TO 1
  432 RATION=Z1(1)
      K=1
      K5=1
  411 IF (Z1(K+1)-Z1(K5)) 412,413,413
  412 K=K+1
      IF (K-LK) 411,414,414
  413 RATION=Z1(K+1)
      K5=K+1
      K=K+1
      GO TO 411
C         THE Z'S ARE NORMALIZED.  THE Z1'S WILL BE NORMALIZED IN THE MAIN PROGRAM.
  414 DO 425 I=1,LLL
  425 Z(I)=Z(I)/RATION
    1 CONTINUE
      RETURN
      END
```

FIGURE 26: (continued)

```fortran
      SUBROUTINE FILTER (OUT,IMIN,IMAX,XSTEP,UO,QQQ,NCOL,KMAX,OUT2)
C     QQQ =  Q OF SYSTEM
C     UO = PASS FREQUENCY
C      XSTEP=DRH,INCREMENT ALONG INVERSE-B AXIS.   KMAX=1,BY STEAD1
C     IMIN = 1 SET BY MAIN.   IMAX=NPTS, USUALLY 10000 OR LESS.
C     MPTS IS USED AS A CONTROL ON WHAT WILL BE GRAPHED
C     NSTRT SPECIFIES FROM WHAT POINT THE HIGH-FIELD INPUT DATA WILL BE USED.
      DIMENSION Z(1001)
      COMMON XLAB(5),YLAB(5),Y(1)
  500 KS=1547714624
      QQ=0.
      QP=0.
      OUT=0.
      OUT2=C.
      K=IMIN
      M=1
   40 H=UO*XSTEP
      IF (H) 4,4,5
    4 H=-H
    5 CONTINUE
C     PARAMETERS   ARE SET UP.
      A1=1.-H*H/2.
      A2=H*(1.-H/(2.*QQQ))
      A3=H*H/2.
      A4=1.-H/QQQ
      A5=-H
  501 I=1
      L=1
      DO 1 J=1,NCOL
    1 Z(J)=0.
C
C     THIS IS THE BASIC PART OF THE FILTER.   THE EQUATIONS APPROXIMATE THE
C     RESPONSE QQ(K) OF A FILTER TO A FORCING FUNCTION Y(K)--THE INPUT DATA.
C           QQ(K+1)  = A1*QQ(K) + A2*QQ'(K) + A3*Y(K)
C           CQ'(K+1) = A4*QQ'(K) + A5*QC(K) + H*Y(K)
```

FIGURE 26:   (continued)

```
C
    6 QQ1=A1*QQ+A2*QP+A3*Y(K)
      QP=A4*QP+A5*QQ+H*Y(K)
      QQ=QQ1
      IF (K-KMAX) 3,15,15
C     KMAX=1 BY STEAD1, SC STEP 15 IS NEXT.
C     THE FILTER OUTPUT IS COLLECTED HERE.   'OUT2' IS THE SUM OF THE SQUARES
C     OF THE AMPLITUDES CF THE RESPONSE.
   15 OUT2=OUT2+QQ*QQ
C     THE PERIODOGRAM IS SET UP HERE.  A RESPONSE AMPLITUDE QQ IS ADDED TO Z(I)
C     EVERY NCOL TIMES.   IF UO COINCIDES WITH A FREQUENCY CONTAINED IN THE DATA,
C     Z(I) WILL BE SUMMED FOR THE SAME PHASE OF THE CYCLE OF QQ EACH TIME, AND
C     THE SUMMATION WILL BE COHERENT.
      Z(I)=Z(I)+QQ
      IF (QQ-30COCO) 71,71,72
   72 WRITE (3,73) OUT2,QQ,K,Y(K)
   73 FORMAT ('    TILT*   OUT2=',E14.3,'QQ=',E15.4,'Y(',I4,')=',E20.4)
      M=M+1
      IF (M-5) 71,71,74
   74 GO TO 9
   71 CONTINUE
      I=I+1
      IF (I-NCOL) 3,3,2
    2 I=1
      L=L+1
    3 K=K+1
      IF (K-IMAX) 6,9,9
C     L COUNTS THE NUMBER OF TIMES A QQ AMPLITUDE IS PLACED IN EACH Z(I).
    9 ZSUM=0.
      DO 10 I=1,NCOL
   10 ZSUM=ZSUM+Z(I)/L
      ZSUM=ZSUM/NCOL
C     L*NCOL = NPTS--ZSUM IS THE AVERAGE PERIODOGRAM RESPONSE Z.
      OUT=0.
C     THE MEAN SQUARE OF THE PERIODOGRAM RESPONSE IS TAKEN, AND CALLED 'OUT'.
```

FIGURE 26:   (continued)

```
      DO 11  I=1,NCOL
   11 OUT=OUT+(Z(I)-ZSUM)**2
      OUT=OUT/NCOL
C     THE FILTER RESPONSE IS 'OUT2'.
      OUT2=OUT2/(IMAX-KMAX)
      RETURN
      END
```

FIGURE 26: (continued)

```
      SUBROUTINE BFIELD (H, IMAX,THETA,HO)
      DIMENSION H(1)
      P=(COS(THETA))**2
      X=HO*(3.*P-1.)/2.
      Y=HO*P
      DO 1 I=1,IMAX
    1 H(I)=HO+H(I)*(H(I)+X)/(H(I)+Y)
      RETURN
      END
```

FIGURE 26: (continued)

```
      SUBROUTINE STEADF(CGQ,MPTS,DRH,H1,THETA,HZERO,HEAD,F1,F2,RES,
     1TIMEM,KMAX,NPTS)
C     THIS SUBROUTINE READS IN THE DHVA DATA Y (DIMENSION OF 4000)
C     AND CALLS STEAD1.
      DIMENSION Y(4000),H(4000),JAZZ(30)
      DIMENSION GLAB1(5),GLAB2(5),HEAD(1)
      DOUBLE PRECISION DRH
      COMMON XLAB(5),YLAB(5),QG(1)
C     THE SECOND CARD IN THE DATA SET IS READ.
C     NOPT=1 IF THE FIELD IS READ ONLY AT START AND STOP--USUAL CASE.
C     NOPT<1 IF THE FIELD IS READ AT EACH DATA POINT.
C     H1 AND H2 ARE THE INITIAL AND FINAL CURRENTS IN THE VARIAN
C     SOLENOID, IN MILLIAMPS.    DELT IS SPECIFIED AS 1.000
C     IF H1 AND H2 ARE ABOVE 20000, THEY SPECIFY FIELD IN OERSTEDS, FROM NMR.
C     F1 AND F2 SPECIFY THE FREQUENCY RANGE SCANNED.
      READ(1,1)NOPT,H1,H2,DTIME,DT1,DELT,F1,F2,RES,TIMEM,MPTS,NSTRT
    1 FORMAT(I2,2F6.0,3F9.3,2E9.2,F6.3,F2.0,I2,I5)
      DO 3 I=1,5
      GLAB1(I)=HEAD(I)
    3 GLAB2(I)=HEAD(I+5)
      IF (MPTS) 30,31,32
   30 WRITE (3,33)
   33 FORMAT ('      NO GRAPHS PLOTTED')
      GO TO 42
   31 WRITE (3,34)
   34 FORMAT ('      INPUT WAVEFORM AND OUTPUT SPECTRA PLOTTED')
      GO TO 42
   32 WRITE (3,35)
   35 FORMAT ('      ONLY THE OUTPUT SPECTRA GRAPHED')
   42 IF (H1 - 20000) 40,40,41
C     THE MAGNET CONSTANT OF 3.0469 GAUSS/MA IS USED.
   40 H1=H1*(3.0469)
      H2=H2*(3.0469)
   41 IF (NOPT) 4,4,11
    4 IO=1
```

FIGURE 26: (continued)

```
      IM=13
    5 READ(1,6)(Y(I),H(I), I=IO,IM)
    6 FORMAT(26A3)
      IF (H(I)) 8,8,7
    7 IO=IO+13
      IM=IM+13
      GO TO 5
    8 I=I-1
      IF (H(I)) 8,8,9
    9 INPTS=I
      DO 10 I=1,INPTS
   10 H(I)=H1*H2*DTIME/((H1-H2)*H(I)+(H2*DELT-H1*DT1))
      GO TO 17
   11 IO=1
      IM=26
   12 READ(1,6) (JAZZ(I), I=1,26)
      CALL MESS (JAZZ)
      DO 2 I=1,26
      KTEMP=IO+I-1
    2 Y(KTEMP)=JAZZ(I)
      I=IM
C     THE CARDS ARE READ ONE AT A TIME.  IF THE LAST TWO 3-DIGIT NUMBERS
C     ON THE CARD ARE ZERO, THE DATA SET IS CONSIDERED TO BE TERMINATED.
C     THEREFORE, IF THE FINAL CARD IN A DATA SET IS FILLED OR HAS ONLY ONE
C     THREE-DIGIT NUMBER MISSING, AN EXTRA BLANK CARD MUST BE INSERTED
C     AFTER IT.
      IF (Y(I)) 13,14,13
   13 IO=IO+26
      IM=IM+26
      GO TO 12
   14 I=I-1
      IF (Y(I)) 13,16,13
   16 I=I-1
      IF (Y(I)) 15,16,15
C     THE TOTAL NUMBER OF INPUT DATA POINTS IS COUNTED, AND IS CALLED
```

FIGURE 26: (continued)

```
C      'INPTS'.   IT IS DIMENSIONED TO 4000.
   15 INPTS=I
      WRITE (3,19)INPTS
   19 FORMAT (64X,'INPTS=',I6)
      T=DT1
      DTIME=INPTS
      I=1
C      THE H-ARRAY IS GENERATED, ASSUMING A UNIFORM, LINEAR RAMP FROM
C      H1 TO H2.
   26 H(I)=((H2-H1)*(T-DT1)/DTIME+H1)
      I=I+1
      T=T+DELT
      IF (I-INPTS)26,26,17
   17 CALL STEAD1 (QQQ,MPTS,DRH,H1,THETA,HZERO,Y,H,INPTS,GLAB1,GLAB2,
     1F1,F2,RES,KMAX,NPTS,NSTRT)
      RETURN
      END
```

FIGURE 26: (continued)

```
      SUBROUTINE STEAD1 (QQQ,MPTS,DRH,H1,THETA,HZERC,Y,H,INPTS,GLAB1,
     1GLAB2,F1,F2,RES,KMAX,NPTS,NSTRT)
C     THIS SUBROUTINE GENERATES THE EVENLY SPACED ARRAY OF DATA IN 1/B.
      DIMENSION X(4000),Y(1),H(1)
      DIMENSION GLAB1(1),GLAB2(1)
      COMMON XLAB(5),YLAB(5),QQ(1)
      DOUBLE PRECISION DRH,T
      KS=1547714624
      IF (HZERO) 19,19,18
   18 CALL BFIELD (H,INPTS,THETA,HZERO)
   19 CONTINUE
C     NSTRT SPECIFIES THE NUMBER OF INPUT DATA POINTS AT THE LOW-FIELD
C     END WHICH WILL BE DISREGARDED.  THIS IMPROVES RESOLUTION OF FRE-
C     QUENCIES HIGHER THAN THE DOMINANT FREQUENCY.
C     IT IS LEFT AS AN EXERCISE TO THE READER TO SHOW THAT THE RESOLUTION
C     IS IMPROVED IF INPUT DATA POINTS ARE THROWN AWAY.
      IF (NSTRT) 51,51,52
   52 JNPTS = INPTS
      INPTS=JNPTS-NSTRT
      IF (H(1)-H(INPTS)) 55,55,56
   56 WRITE (3,57)NSTRT
   57 FORMAT ('    COUNT STOPS AT PT',I6)
      GO TO 51
   55 DO 53 I=1,INPTS
      J=I+NSTRT
      Y(I)=Y(J)
   53 H(I)=H(J)
      WRITE (3,58)NSTRT
   58 FORMAT('    COUNT STARTS AT PT',I6)
   51 WRITE (3,54)H(1),H(INPTS),INPTS
   54 FORMAT('    FIELD RANGE IS ',2F9.1,'INPTS=',I6)
      H1=H(1)
C     THE FIELD ARRAY IS INVERTED.
      DO 20 I=1,INPTS
   20 H(I)=1./H(I)
```

FIGURE 26: (continued)

```
      IF (F1) 40,40,41
   40 NCALC=50
      NCYC1=11
      NCYC2=INPTS-NCYC1+1
      F2=1.20*(NCYC1-1)/((H(NCYC1) -H(1))*2.)
      F1=0.80*(NCYC1-1)/((H(INPTS)-H(NCYC2))*2.)
      RES=(F2/F1)**(1./NCALC)-1
   41 CONTINUE
      NPTS = 10000
      IF (RES) 6,6,11
C     THE FREQUENCY RESOLUTION IS COMPUTED.    THAT IS, DISTANCE IN 1/B
C     SPACE IS MULTIPLIED BY THE HIGHEST FREQUENCY SOUGHT.   DIVIDING BY
C     NPTS GIVES THE FRACTION OF A CYCLE OF F2 BETWEEN TWO SUCCESSIVE DATA
C     POINTS AND THUS TO WHAT PERCENTAGE F2 CAN BE RESOLVED.
C     THE RESOLUTION TYPICALLY IS OF THE ORDER OF 1%.
    6 RES=(H(INPTS)-H(1))*F2/NPTS
      IF (RES) 10,10,11
   10 RES=-RES
C     DRH IS THE INCREMENT IN 1/B SPACE.
   11 DRH=(H(INPTS)-H(1))/NPTS
  675 C12=0.
      DO 27 I=1,INPTS
   27 C12=C12+Y(I)
      W= INPTS
      C12=C12/W
      DO 28 I=1,INPTS
   28 Y(I)=Y(I)-C12
      K=1
      I=1
      T=H(1)
C     HERE THE ACTUAL DATA ARRAY QQ IS GENERATED.   THE POINTS QQ(FCTN OF 1/B)
C     ARE SPACED BY INCREMENTS OF DRH IN 1/B SPACE, AND ARE FOUND BY INTER-
C     POLATING BETWEEN THE TWO NEAREST INPUT DATA POINTS.    THIS ARRAY
C     QQ IS CONNECTED THROUGH COMMON TO THE Y ARRAY IN 'FILTER'.
   21 QQ(K)=(Y(I+1)-Y(I))*(T-H(I))/(H(I+1)-H(I))+Y(I)
```

FIGURE 26:   (continued)

```
      K=K+1
      T=T+DRH
      IF (DRH) 22,22,24
   22 IF (T-H(I+1)) 23,21,21
   23 I=I+1
      IF (I-INPTS)21,26,26
   24 IF (T-H(I+1)) 21,21,30
   30 I=I+1
      IF (I-INPTS)21,26,26
   26 CONTINUE
      KMAX=1
C     THE NUMBER K (=NPTS) OF INTERPOLATED DATA POINTS IS NOTED.
      WRITE(3,987) K
987   FORMAT(64X,'K=',I10)
      IF (DRH) 1,2,2
    1 DRH = -DRH
    2 CONTINUE
      IF (MPTS) 32,31,32
   31 DO 29 I=1,INPTS
      X(I)=I/2.
   29 H(I)=H(I)*10.**7
      CALL GRAPH(INPTS,X,Y,KS,4,12., 10.,0,0,0,0,XLAB,YLAB,GLAB1,GLAB2)
      CALL GRAPH(INPTS,X,H,KS,4,0.,10.,0,0,0,0,0,0,0,0)
C     NOW RETURN TO 'MAIN'.
   32 CONTINUE
      RETURN
      END
```

FIGURE 26: (continued)

```
      SUBROUTINE MESS (JAZZ)
C         THIS ROUTINE TRANSLATES THE FIRST 26 ELEMENTS CF THE ARRAY
C         JAZZ FROM THREE CIGIT NUMERIC WITH A MINUS PUNCH OVER THE
C         HIGH ORCER DIGIT IF NEGATIVE (THAT WERE READ UNDER AN
C         A3 FORMAT CODE) INTO NORMAL INTEGERS.
C      ALSO CHECKS FOR - PUNCH ONLY AS A HIGH CRDER DIGIT.
C         THIS ROUTINE IS COMPLETELY IBM 360 MACHINE DEPENDENT
       DIMENSION JAZZ(26),Y(1)
       DO 100 I=1,26
       NA=JAZZ(I)
       L=1
       N=0
       IF (NA) 2,5,5
    5  IF (NA-1077952576) 2,80,2
    2  DO 4 J=1,3
       IF (NA) 40,30,30
   30  L=-1
       GO TO 4
   40  M=NA/16777216+15
       IF (M) 3,60,60
    3  L=-1
       M=M+32
   60  N=N*10+M
    4  NA=NA*256
   80  JAZZ(I)=ISIGN(N,L)
  100  CONTINUE
       RETURN
       END
```

X.   APPENDIX II.

FIGURE 27: A program for analysis of dHvA frequencies using the fast Fourier transform subroutine "RHARM".

```
C       DHVA FREQUENCY ANALYSIS PROGRAM USING FAST FOURIER ANALYSIS SUBROUTINE.
C
        DOUBLE PRECISION DRH
        DIMENSION UU1(100),Z1(100),Z(400)
        DIMENSION UU(400)
        DIMENSION HEAD(10)
        DIMENSION XLAB1(5),YLAB1(5),GLAB1(5),GLAB2(5)
        DIMENSION ARRAYT(7)
        DIMENSION INV(2400), S(2400)
        COMMON XLAB(5),YLAB(5),Y(8200)
        KS=1547714624
        IMIN=1
        LMAX=0
        OUTRA=10.**30
        READ (1,6) XLAB,YLAB,XLAB1,YLAB1
6 FORMAT (20A4)
1 FORMAT (2F5.0,3F6.0,2F4.0,2I2,10A4)
2 FORMAT ('1     DE HAAS-VAN ALPHEN COMPUTATIONS--    DATA SET NUMBER
  1',12A4)
3 FORMAT ('0     RATE=',F4.0,' KCPS.     HSCALE=',F6.4,'       HZERO=',F6.0
  1,' GAUSS    THETA=',F7.2,' DEG.       COILK=',F6.0,' GAUSS/VOLT     TZE
  1RO=',F4.0,' MSEC.')
4 READ (1,1) RATE,HSCALE,HZERO,THETA,COILK,TZERO,QQQ,MPTS,NADD,
  1(HEAD(I),I=1,10)
5 WRITE (3,2) (HEAD(I),I=1,10)
9 DO 8 I=1,5
    GLAB1(I)=HEAD(I)
8 GLAB2(I)=HEAD(I+5)
    DELT=0.0
    CALL STARTM(DELT)
    HSCALE=HSCALE/10000.
    THETA=THETA/100.
    WRITE (3,3) RATE,HSCALE,HZERO,THETA,COILK,TZERO
    PIE=3.14159
    TZERO=TZERO/(10.**6)
```

FIGURE 27:   (continued)

```
      THETA=THETA*PIE/18C.
      NDEG=3
      IF (QQQ) 731,731,732
731   QQQ=1C.
732   CONTINUE
      CALL CATE(ARRAYT)
      WRITE (3,103) ARRAYT
103   FORMAT (4X,7A4)
      IF (RATE) 300,200,100
100   DT=1./(RATE*1000.)
      GO TO 4C0
200   CONTINUE
      GO TO 400
300   CALL STEADF (QQQ,MPTS,DRH,H1,THETA,HZERO,HEAD,FFIRST,FLAST,RES,
     1TIMEM,KMAX,NPTS)
400   CONTINUE
      RES1=RES*100.
601   FORMAT ('0            LOWEST FREQUENCY CONSIDERED WAS  =',E10.3)
602   FORMAT ('             HIGHEST FREQUENCY CONSIDERED WAS =',E10.3)
      WRITE (3,601) FFIRST
      WRITE (3,602) FLAST
419   FORMAT (' ')
      M = 12
      FACTOR=1./(2.*NPTS*DRH)
      CALL RHARM (Y,M,INV,S,IFERR)
      KLAST=FLAST/FACTOR
      KFIRST=FFIRST/FACTOR
      J=0
608   FORMAT ('   KFIRST=',I6,'  KLAST=',I6)
      WRITE (3,608) KFIRST,KLAST
      DO 500 K=KFIRST,KLAST,2
      J=J+1
      Z(J)=(Y(K))**2 + (Y(K+1))**2
      W = K
500   UU(J)=FACTOR*W
```

FIGURE 27: (continued)

```
      CALL FIT (J,Z,UU,UU1,Z1,RATION,LK)
      DO 418 I=1,LK
 418 Z1(I)=Z1(I)/RATION
 426  CALL GRAPH ( J ,UU,Z, 3, 3,12.,10.,0,C,0.1,00.0,XLAB1,YLAB1,
    1GLAB1,GLAB2)
 428 WRITE (3,415) RATION
 415 FORMAT ('         NORMALIZING FACTOR (FAST FOURIER FIT)  =',E10.3)
      WRITE (3,416)
 416 FORMAT ('0')
 417 FORMAT ('0            FREQUENCY           INTENSITY')
      WRITE (3,1002)
1002 FORMAT ('0         FAST FOURIER FIT ANALYSIS')
      WRITE (3,417)
      WRITE (3,419)
      I=1
      LLLLK=LK
 800 IF (Z1(I)-0.01) 801,802,802
 802 I=I+1
      IF (I-LLLLK) 800,800,820
 801 IF (I-LLLLK) 804,806,806
 804 LLLLK=LLLLK-1
      DO 803 K=I,LLLLK
      Z1(K)=Z1(K+1)
 803 UU1(K)=UU1(K+1)
      GO TO 800
 806 LLLLK=LLLLK-1
 820 DO 420 I=1,LLLLK
 420 WRITE (3,421) UU1(I),Z1(I)
 421 FORMAT (E20.5,E19.5)
 461 CONTINUE
      CALL STOPTM(DELT)
      WRITE (3,699) DELT
 699 FORMAT (62X,'  TIME USED IN EXECUTION   (SEC)', F8.2)
      QQQ=0.
      F1=0.
```

FIGURE 27: (continued)

```
      F2=0.
      RES=0.
      MPTS=0
      READ (1,1) RATE,HSCALE,HZERO,THETA,COILK,TZERO,QQQ,MPTS,NADD,
     1(HEAD(I),I=1,10)
  501 IF (RATE) 5,450,5
  450 IF (COILK) 5,451,5
  451 WRITE (3,452)
  452 FORMAT ('1            END OF DATA    PANOUSIS   220 RES.   TELE 4-6816')
C     THE ONLY CHANGE IN THE OTHER SUBROUTINES IS TO SET NPTS TO BE A
C     POWER OF 2 FOR THE USE OF RHARM.   STEADF SETS NPTS TO 8192.
      STOP
      END
```